



**HAL**  
open science

## **Integrated astrochronology of the Barremian Stage (Early Cretaceous) and its biostratigraphic subdivisions**

Mathieu Martinez, Roque Aguado, Miguel Company, Jose Sandoval, Luis  
O'Dogherty

► **To cite this version:**

Mathieu Martinez, Roque Aguado, Miguel Company, Jose Sandoval, Luis O'Dogherty. Integrated astrochronology of the Barremian Stage (Early Cretaceous) and its biostratigraphic subdivisions. *Global and Planetary Change*, 2020, 195, pp.103368. 10.1016/j.gloplacha.2020.103368 . insu-02987662

**HAL Id: insu-02987662**

**<https://insu.hal.science/insu-02987662>**

Submitted on 4 Nov 2020

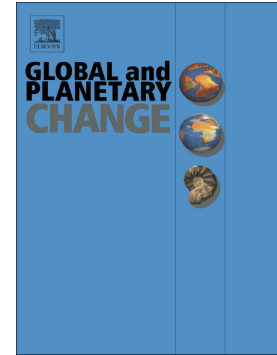
**HAL** is a multi-disciplinary open access archive for the deposit and dissemination of scientific research documents, whether they are published or not. The documents may come from teaching and research institutions in France or abroad, or from public or private research centers.

L'archive ouverte pluridisciplinaire **HAL**, est destinée au dépôt et à la diffusion de documents scientifiques de niveau recherche, publiés ou non, émanant des établissements d'enseignement et de recherche français ou étrangers, des laboratoires publics ou privés.

## Journal Pre-proof

Integrated astrochronology of the Barremian Stage (Early Cretaceous) and its biostratigraphic subdivisions

Mathieu Martinez, Roque Aguado, Miguel Company, Jose Sandoval, Luis O'Dogherty



PII: S0921-8181(20)30259-9

DOI: <https://doi.org/10.1016/j.gloplacha.2020.103368>

Reference: GLOBAL 103368

To appear in: *Global and Planetary Change*

Received date: 7 February 2020

Revised date: 27 October 2020

Accepted date: 27 October 2020

Please cite this article as: M. Martinez, R. Aguado, M. Company, et al., Integrated astrochronology of the Barremian Stage (Early Cretaceous) and its biostratigraphic subdivisions, *Global and Planetary Change* (2020), <https://doi.org/10.1016/j.gloplacha.2020.103368>

This is a PDF file of an article that has undergone enhancements after acceptance, such as the addition of a cover page and metadata, and formatting for readability, but it is not yet the definitive version of record. This version will undergo additional copyediting, typesetting and review before it is published in its final form, but we are providing this version to give early visibility of the article. Please note that, during the production process, errors may be discovered which could affect the content, and all legal disclaimers that apply to the journal pertain.

© 2020 Published by Elsevier.

## **Integrated astrochronology of the Barremian Stage (Early Cretaceous) and its biostratigraphic subdivisions**

Mathieu Martinez<sup>1</sup>, Roque Aguado<sup>2</sup>, Miguel Company<sup>3</sup>, Jose Sandoval<sup>3</sup>, Luis O'Dogherty<sup>4</sup>

<sup>1</sup>*Univ Rennes, CNRS, Géosciences Rennes, UMR 6118, 35000 Rennes, France*

<sup>2</sup>*Departamento de Geología y CEACTEMA, Universidad de Jaén, Campus Científico-Tecnológico de Linares, 23700 Linares, Spain*

<sup>3</sup>*Departamento de Estratigrafía y Paleontología, Universidad de Granada, 18002 Granada, Spain*

<sup>4</sup>*Departamento Ciencias de la Tierra, Universidad de Cádiz, CASEM, 11510 Puerto Real, Spain*

Corresponding author: Mathieu Martinez (mathieu.martinez@univ-rennes1.fr)

### **Abstract**

The ages and durations of the stages in the Early Cretaceous commonly show discrepancies of several million years when the Geologic Time Scale (2020) from the International Commission of Stratigraphy (ICS) and recently published radio-astrochronologic data are compared. Here, we provide an astronomical time scale for the Barremian Stage and its subdivisions based on spectral analyses performed on magnetic susceptibility and calcium carbonate content series in two sections studied located in the Subbetic Domain of southeastern Spain. The sections are tied to Tethyan ammonite and calcareous nannofossil zones, allowing detailed correlations with other sections in the Subbetic Domain and other basins in the Tethyan Realm. Eccentricity cycles are observed throughout the series and can be correlated with the eccentricity cycles observed in other sections in the Subbetic Domain, showing that the results are reproducible. Based on the number of 405-kyr eccentricity cycles in the study interval, and considering uncertainties linked to variations in the sedimentation

rates within an eccentricity cycle, the duration of the Barremian Stage is calculated at  $4.58_{-0.29}^{+0.15}$  Myr. From the astronomical time scale proposed here, together with recently published radio-astrochronological studies, the base of the Barremian Stage is dated at  $125.98 \pm 0.21$  Ma and the top at  $121.40 \pm 0.34$  Ma. The age of the Barremian/Aptian boundary differs from the ICS Geologic Time Scale 2020 by 3.6 Myr, but fits with the age of the base of magnetochron M0r recently deduced from a synthesis of radiochronologic data. The episodes of environmental change of the late Hauterivian–Barremian show an average pacing of 2.2 Myr, suggesting an orbital control on the expansion of oceanic anoxic conditions in the Tethys.

**Keywords:** Barremian Stage; Early Cretaceous astrochronology; Milankovitch; Episodes of Environmental Change; Geologic Time Scale

## 1. Introduction

Numerous discrepancies have been reported between the successive versions of the Geologic Time Scale from the International Commission of Stratigraphy (ICS; Cohen et al., 2013 and updates; <https://stratigraphy.org/chart>) and Early Cretaceous radio-astrochronologic studies (Aguirre-Urreta et al., 2015, 2017, 2019; Martinez et al., 2013, 2015; Lena et al., 2019). In the last 5 years, these studies have shown younger ages and reassessed the durations from the Berriasian to the Hauterivian stages, with ages and durations differing by several million years compared to compiled Geologic Time Scales (Gradstein et al., 2012; Cohen et al., 2013; Ogg et al., 2016). These revised time scales notably demonstrated the synchronicity between the Weissert Event (mid-Valanginian) and the Paraná-Etendeka Large Igneous Province (Martinez et al., 2015) and show the age of the Jurassic-Cretaceous boundary is

several million years younger than in the ICS Geologic Time Scale 2020 (Vennari et al., 2014; Lena et al., 2019). As the ages show much less uncertainties in the early Late Cretaceous (e.g., Meyers et al., 2012; Batenburg et al., 2016; Thibault et al., 2016), the duration of the interval from the Barremian to the Albian stages is likely overestimated in the current Geologic Time Scale. To date, no radiometric age is described within the Barremian Stage (Gradstein et al., 2012), and the duration of the Barremian Stage relies on cyclostratigraphic studies in the Vocontian Basin (SE France; Bodin et al., 2006a) and the Maiolica Formation from the Umbria-Marche Basin (Central Italy; Fiet and Gorin, 2000; Bodin et al., 2006a; Sprovieri et al., 2006). Fiet and Gorin (2000) and Bodin et al. (2006a) calculated the duration of the Barremian Stage from counting bed cycles visually identified and respectively attributed to the precession and the short eccentricity (~100 kyr) cycles. Their durations range from 4.5 Myr to 5.1 Myr. In the Vocontian Basin, the marl-limestone alternations evolve to a succession of massive limestone beds in the middle of the Barremian Stage which may hinder the identification of the precession cycles. In the Maiolica Formation, bed stacking, as visually identified, can be somewhat subjective in intervals of massive limestone beds and can lead to overestimation of the number of cycles. Spectral analyses performed on the low-resolution  $\delta^{13}\text{C}$  curve to identify the 405-kyr eccentricity cycle is problematic (Sprovieri et al., 2006), as the 405-kyr cycle may be distorted by the residence time of carbon in pelagic domains (Laurin et al., 2017), and no shorter cycle was identified in Sprovieri et al. (2006) to confirm the cycle assignment and duration assessment.

The marl-limestone alternations of the Subbetic Domain (SE Spain) faithfully record the orbital cycles in magnetic susceptibility (MS), Gamma-Ray Spectrometry (GRS),  $\text{CaCO}_3$  content, and clay mineral assemblages (Sprenger and Ten Kate, 1993; Martinez et al., 2012; Moiroud et al., 2012; Martinez, 2018). They were notably the consequence of humid-arid cycles forced by insolation cycles (Moiroud et al., 2012). High amount of macro- and

microfossils allow the Tethyan ammonite and calcareous nannofossil zones and subzones to be precisely bounded (Hoedemaeker and Leereveld, 1995; Company et al., 2003b; Aguado et al., 2014a). The quality of the record of the Milankovitch cycles in the Subbetic Domain represents an opportunity to provide much more precise constraint on the duration of the Barremian Stage that can be integrated in a broader stratigraphic scheme. Notably, strata in the Subbetic Domain can be correlated sometimes bed-to-bed with other sections in the Subbetic Domain (Company et al., 2003a, b; Aguado et al., 2014a) and with the Vocontian Basin (Hoedemaeker and Hergreen, 2003). We here performed spectral analyses on high-resolution magnetic susceptibility and  $\text{CaCO}_3$  content curves in two sections of the Subbetic Domain to identify the record of the Milankovitch cycles and precise the duration of the Barremian Stage and its biostratigraphic subdivisions.

## 2. Geological setting

The two sections studied here (Arroyo Gilico and Barranco de Cavila) are both located in the province of Murcia (SE Spain). The Arroyo Gilico section (coded X.V1) is located on a small foothill north of the Carabones Mountain, 13 km NE of Cehegín and 8 km SSE of Calasparra (geographical coordinates:  $38^{\circ}9'35''$  N  $1^{\circ}40'41''$  W). The Barranco de Cavila section (coded X.Kv2) crops out on the slope between the RM-730 regional road and the Cavila gully, some 6 km SSW of Caravaca (geogr. coord.:  $38^{\circ}3'10''$  N  $1^{\circ}53'20''$  W).

Arroyo Gilico is a 75-m thick section, which stratigraphically ranges from the uppermost Hauterivian to the lowermost upper Barremian. Data on ammonite, calcareous nannofossil and planktic foraminifera biostratigraphy and isotope stratigraphy of this section have been published in several previous papers (Company et al., 2003a; Aguado et al., 2008, 2014a; Premoli Silva et al., 2018). Barranco de Cavila is a 70-m thick section covering the

upper Barremian and the lowermost Aptian. The ammonite distribution around the Barremian-Aptian boundary in this section was described in Aguado et al. (1997).

From biostratigraphy and carbon isotope stratigraphy, two stratigraphic equivalents of paleoceanographic events have been identified in the Arroyo Gilico section: the Faraoni and the Mid-Barremian events. The Faraoni Level was first defined in the Umbria-Marche Basin (Central Italy) as organic-rich levels at the base of the Mortilleti Subzone (Baudin et al., 1998). The LO of *L. bollii* also occurs within this event and biostratigraphic turnovers have been identified (Company et al., 2005). Stratigraphically-equivalent organic-rich beds were then identified throughout the Western Tethys, including the Río Argos section (Baudin, 2005; Baudin and Riquier, 2014). From biostratigraphy and micropalaeontology, the Faraoni equivalent levels are also identified in the Arroyo Gilico section (Aguado et al., 2014a). The Mid-Barremian Event, defined in the Umbria-Marche Basin as an increase in organic-rich deposits, corresponds to an increase in the  $\delta^{13}\text{C}_{\text{carb}}$  values in the late early Barremian (Sprovieri et al., 2006; Föllmi et al., 2012). In the Arroyo Gilico section, this increase in  $\delta^{13}\text{C}_{\text{carb}}$  values occurs in the Moutonianum Zone and is associated to an episode of increased runoff, humid conditions and eutrophication of the upper water column (Aguado et al., 2014a; Fig. 2).

From a geological point of view, both sections belong to the Subbetic Zone (Fig. 1C), a complex unit that roughly corresponds to the pelagic domain of the southern passive paleomargin of the Iberian Plate during the Alpine tectonic cycle (Triassic to Early Miocene; Fig. 1A). The morphology of this Subbetic Basin was quite irregular due to a severe intracontinental rifting, which gave rise to well-defined swells and troughs bordered by extensional faults that were tectonically active during the Jurassic and the Early Cretaceous (Vera, 2001; Vera et al., 2004; Fig. 1E).

The lithologic successions are similar in the two sections, and made of a rhythmic alternation of marly limestone beds (5-75 cm thick) and marlstone interbeds (10-600 cm thick)

(Fig. 1B), belonging to the Miravetes Formation (van Veen, 1969). Texturally, these sediments are mudstones and wackestones with radiolarians and foraminifers. Macrofossil remains are common, being dominated by ammonites, accompanied by scarce belemnites, bivalves, gastropods, brachiopods and irregular echinoids. These sedimentological and palaeontological features indicate that the Arroyo Gilico and Barranco de Cavila successions were deposited in a stable, low-energy, relatively deep-water environment. The Arroyo Gilico section would have corresponded to a more proximal and less subsident area in the basin than the Barranco de Cavila section (de Gea, 2004; Aguado et al., 2014a; Fig. 1E). Spectral analyses performed on clay minerals,  $\text{CaCO}_3$  content, magnetic susceptibility and gamma-ray spectrometry demonstrated the imprint of the Milankovitch cycles in these marl-limestone alternations (Sprenger and Ten Kate, 1993; Martinez et al., 2012, 2015; Moiroud et al., 2012). Higher contents in kaolinite and illite clay minerals in marls point out tropical, annually humid conditions during marl deposits, while limestone beds were deposited under more arid, seasonally-contrasted conditions (Fig. 1D).

### 3. Material and methods

#### 3.1. Magnetic susceptibility (MS)

Bulk-rock samples were collected every 0.07 m in the Arroyo Gilico and the Barranco de Cavila sections, totalling 2027 samples. The sample distance was selected to ensure at least 7 points per marl-limestone alternations, as recommended to preserve the quality of the record of high frequencies (Herbert, 1994). Regularity of sampling was ensured thanks to a Jacob's staff to limit the errors in the sample position which can impact the spectrum at high frequencies (Martinez et al., 2016). Samples were cleaned, their weathered surface was removed and weighted prior to MS measurements. Samples have a mean weight of 15 g in

Arroyo Gilico and 18 g in Barranco de Cavila. The volumic MS measurement was conducted with an Agico KLY-3 at the University of Rennes. Measurements were corrected from blank values and normalized to sample mass. Assuming a measurement volume of  $10 \text{ cm}^3$ , the massic MS are given in  $\text{m}^3 \cdot \text{kg}^{-1}$ . Replicates were done on 252 samples (*ca.* 1/8 samples). On average, the variability of the MS measurements is 1 % ( $2\sigma$ ) of the MS value.

### 3.2. Carbonate calcium content ( $\text{CaCO}_3$ content)

Unweathered fractions of all samples collected for magnetic susceptibility, lacking diagenetic veins, were dried and ground to powder and homogenized in an agate mortar. The carbonate content of all bulk rock samples was determined, by volumetric method (following ASTM D-4373-02 standard), at the Geology Department of EPS Linares. Samples were processed using the automatic calcimeter Dr am Électronique, with a range of masses 90–150 mg and measurement time of 20 s at a temperature of  $20 \pm 2 \text{ }^\circ\text{C}$ . This guarantees a maximum error in the determination of the carbonate content of  $\pm 4 \%$ .

### 3.3. Carbon and oxygen isotopes

For the Arroyo de Gilico section, the stable isotope ratios obtained on 113 samples are shown in Figure 2 and correspond to data already published in Aguado et al. (2014a). A total of 47 samples from the Barranco de Cavila section have been analyzed in this study for carbon and oxygen isotope ratios (Fig. 3). For this latter section, analyses were made on bulk carbonate samples from limestones, or marly limestones. The samples were prepared by removing the outermost 2 cm from the rock, and then drilled on a fresh surface with a diamond coated micro-drill bit. Alteration crusts and secondary mineralization features were carefully avoided in order to obtain results representative of the whole rock. Carbon and

oxygen isotopes were measured on a Wahlen VG Prism II Mass Spectrometer equipped with an automated carbonate preparation module at the Isotope Geochemistry Laboratory of Zurich University. Samples were reacted in 100 % phosphoric acid at 90° C to obtain CO<sub>2</sub>. The mass spectrometer was calibrated with three NBS standards, Nos. 18, 19 and 20. The analytical reproducibility is better than  $\pm 0.1$  ‰ for carbon and oxygen, based on repeated measurements of a laboratory-internal standard (Carrara marble) calibrated against NBS standards. The isotopic compositions are reported in standard delta notation relative to Vienna PeeDee Belemnite (VPDB).

#### *3.4. Ammonites*

Every limestone bed of both sections was sampled for ammonites, and almost all were productive. More than 6000 specimens (452 from the Arroyo Gilico section and 1540 from the Barranco de Cavila section) were collected and most of them could be taxonomically identified at the species level. The material is stored in the paleontological collections of the University of Granada.

As mentioned above, the stratigraphic interval studied spans the uppermost Hauterivian-lowermost Aptian interval. Almost all the main stratigraphic units of the current standard ammonite zonation for the Mediterranean Province (Reboulet et al., 2018) comprised in this interval were recognized.

#### *3.5. Calcareous nannofossils*

Fractions of the same samples collected for the determination of carbonate content and magnetic susceptibility were used for calcareous nannofossil biostratigraphy. Marlstone

samples were preferred over limestones, as usually they provide better preserved calcareous nannofossil assemblages. A total of 305 samples (83 from the Arroyo Gilico section and 222 from Barranco de Cavila section) were selected for calcareous nannofossil investigation, in order to determine the stratigraphic ranges of the zonal markers with the highest available precision.

Simple smear slides of the selected samples (Bown and Young, 1998) were prepared and mounted with adhesive. Particle density on the slide surface was kept between 40–50 % (Baccelle and Bosellini, 1965), which guarantees that ~1800–2400 microparticles were investigated in each field of view. The smear slides were examined using an Olympus BHSP polarizing light microscope at 1200 × magnification. At least a complete longitudinal traverse (1 traverse = 200 fields of view; 1 field of view =  $2.37 \times 10^{-2} \text{ mm}^2$ ), and occasionally up to 5, were investigated for each sample. The taxonomic framework was based on Perch-Nielsen (1985), Bown et al. (1998), Aguado et al. (2000, 2014b), Bown (2005), and Nannotax website (<http://www.mikrotax.org/Nannotax3/>).

### 3.6. Spectral analyses

Prior to spectral analyses, the series were linearly resampled every 0.07 m, applying an optimized algorithm to limit the difference between the original and the resampled curve which can impact the high frequencies (Martinez et al., 2016). The long-term trend of the data was removed using a best-fit linear regression or the LOWESS method (Locally Weighted Scatterplot Smoothing; Cleveland et al., 1979). In the LOWESS method, a coefficient, ranging from 0 to 1, defines the proportion of the series on which the local smoothing is calculated. The most appropriate method and LOWESS coefficients were selected by comparing the spectrum before and after detrending to ensure that this process did not

generate artificial spectral peaks at frequencies near 0 (see Vaughan et al., 2011), while not affecting higher frequencies already appearing in the spectrum before detrending.

Spectral analyses were done using the multi-taper method (MTM; Thomson, 1982, 1990) applying three  $2\pi$ -tapers. Robust red-noise models were calculated applying linear fits to the spectra. A median smoothing of this red-noise model was applied over 20 % of the spectrum (Mann and Lees, 1996) with a constant end-rule. Confidence levels were calculated assuming a  $\chi$ -squared distribution of the  $p$ -value (Mann and Lees, 1996). In addition, Time-Frequency Weighted Fast Fourier Transforms (T-F WFFTs) were applied to observe the evolution of the periods throughout the studied series (Martinez et al., 2013, 2015). The choice of the window width depended on the longest period to document.

Correlation Coefficient (COCO) was applied to provide an assessment of how well the sedimentary frequency fit with the astronomical periods (Li et al., 2018). The Correlation Coefficient method (Li et al., 2018) calculates the coefficient correlation between the spectrum of the astronomical period, from Waltham (2015), here at 125 Ma, and the spectrum of the sedimentary series at a given sedimentation rate. The COCO method was applied on a large range of sedimentation rates. In every section, the lowest sedimentation rate tested was fixed at  $0.7 \text{ cm.kyr}^{-1}$ , which is the minimum sedimentation rate at which the precession could be detected accounting for the sample distance ( $= 0.14 \text{ cm} / 18 \text{ kyr}$ ). The highest sedimentation rate tested was chosen conservatively high compared to previous duration assessments. The step between two successive sedimentation rates tested was fixed at  $0.01 \text{ cm.kyr}^{-1}$ . The evolutive COCO analysis was also applied to follow the evolution of the sedimentation rate through the series studied. In each test, a total of 10,000 Monte Carlo simulations were applied.

Filters were applied on bands of interest using Taner filters (Taner, 2003). The orbital calibration was made assuming a constant sedimentation rate between each repetition of the target cycle.

## 4. Biostratigraphy

### 4.1. Ammonite biostratigraphy

The Arroyo Gilico section spans the stratigraphic interval between the upper Hauterivian Balearis Zone and the lowermost upper Barremian Vandenheckii Zone. Ammonites are abundant, diverse and well preserved throughout this section making easy the identification of the successive zones and subzones (see Fig. 2), which have all been recognized by the presence of their index species.

The Barranco de Cavila section extends from the Vandenheckii Zone (base of the upper Barremian) to the Forbei Zone (lower Aptian; Fig. 3). In comparison with the Arroyo Gilico section, ammonites are not so abundant and well preserved, which has posed some difficulties for the stratigraphic interpretation that will be discussed next. The Vandenheckii Zone is well constrained by the presence of *Heinzia sayni* at the base of the section (bed 58, 0 m; see detailed logs in supplement for the bed numbers) and the FAD of *Gerhardtia sartousiana* (bed 75, 16 m), but the Alpinum Subzone cannot be recognized due to the absence of its index species (*Gassendiceras alpinum*). Nevertheless, the last occurrence in bed 69 (9 m) of holcodiscids (*Holocodiscus* gr. *uhligi*), which in Arroyo Gilico and other sections of SE Spain is consistently recorded in the higher part of the Vandenheckii Subzone, suggests that the base of the overlying Alpinum Subzone should be placed around beds 70–71 (~10.5 m).

The Sartousiana Zone occupies the interval between the FAD of the index species (*Gerhardtia sartousiana* in bed 75, 16 m) and the FAD of *Imerites giraudi*. In the current standard zonation, this zone is subdivided into a lower Sartousiana Subzone, a middle Provincialis Subzone and an upper Feraudianus Subzone. The FAD of *Gerhardtia provincialis* has been recorded in bed 81 (27 m), but the index species of the upper subzone (*Hemihoplites feraudianus*) has not been found. However, the occurrence in bed 86 (37.1 m) of specimens belonging to the genus *Heteroceras*, whose FAD has been reported from the upper part of the Feraudianus Subzone (Delanoy, 1997; Company et al., 2004), leads us to draw the base of this subzone a few meters below (base of bed 85, 35.1 m).

The Giraudi Zone is poorly represented. The FAD of the index species (*Imerites giraudi*) takes place in bed 88 (44.3 m), but the absence of characteristic ammonites has hindered a more detailed subdivision of this zone. This is also the case of the Sarasini Zone. Its index species (*Martelites sarasini*) has been first recorded in bed 90 (47.4 m), but ammonites become rare and stratigraphically little significant in higher levels. Thus, we have not been able to identify with certainty the Barremian-Aptian boundary. The first Aptian diagnostic ammonites (*Deshayesites forbesi* in bed 102, 61.2 m) characterize the second zone of the Aptian (Forbesi Zone) in the current standard zonation. The first occurrence of *D. forbesi* correlates with a local maximum in the  $\delta^{13}\text{C}_{\text{carb}}$ , which characterizes the boundary between the Oglanlensis and the Forbesi zones in Cassis-La Bédoule and Angles (Bodin et al., 2015; Frau et al., 2018a). The negative excursion in the  $\delta^{13}\text{C}_{\text{carb}}$  curve from bed 94 (50.6 m) to 100 (61.9 m) is probably related with the Taxy Episode and is attributed to the middle-upper Sarasini Zone (Frau et al., 2018a). Thus, in the absence of any other direct biostratigraphic evidence, we positioned the Barremian-Aptian boundary in bed 100 (61.9 m), above the negative excursion in the  $\delta^{13}\text{C}_{\text{carb}}$  curve and below the increase in the  $\delta^{13}\text{C}_{\text{carb}}$  values in agreement with the interpretation of Frau et al. (2018a). We define an uncertainty zone in this

correlation which ranges from the base of bed 98 (at level 56.7 m) to the top of bed 100 (at level 62.2 m) to account for the resolution of the carbon-isotope curve in Barranco de Cavila.

#### 4.2. Calcareous nannofossil preservation and biostratigraphy

All selected samples contained calcareous nannofossils, and preservation allowed determining the biostratigraphically important taxa in all cases. Preservation fluctuates between moderate (uppermost 2 m of the Arroyo Gilico section and lowermost 11 m of the Barranco de Cavila section) to good–moderate (~32–40 m and 48–61 m of the Barranco de Cavila section). Throughout most of the Arroyo de Gilico, and across the intervals 11–32 m, 40–48 m, and 61 m to the top of the Barranco de Cavila section, preservation is moderate–good. Assemblages show a marked Tethyan influence, with common to abundant neritic taxa as *Nannoconus* and *Micrantholithus*.

Previous calcareous nannofossil biostratigraphic data on the Arroyo Gilico section were provided in Aguado et al. (2014). However, several new samples were studied in order to increase the accuracy of the zonal boundaries taking advantage of the new high-resolution sampling performed in this work. The successive record of the last occurrences (LO) of *Lithraphidites bollii* (sample X.V1-206, 14.8 m; see detailed logs in supplements for the position of the samples) and *Calcicalathina oblongata* (sample X.V1-577, 41.3 m) together with the first occurrence (FO) of *Flabellites oblongus* (sample X.V1-826, 57.9 m) in the Arroyo de Gilico section, allowed the determination of NC5B (*p.p.*), NC5C, NC5D, and NC5E (*p.p.*) subzones of Bralower et al. (1995). In addition, the LO of *Micrantholithus spinulentus* (sample X.V1-445, 31.9 m) and the FO of rare specimens of *Lithraphidites* sp. cf. *L. magnus* (sample X.V1-1034, 72.1 m), a new species that will be described in a forthcoming paper, were also recorded throughout the Arroyo de Gilico section (Fig. 2). These two bioevents have shown biostratigraphic potential, being recorded from equivalent stratigraphic

levels in several Barremian sections of the Subbetic basin (Aguado et al., 2014a; 2017; pers. observations), and could be used to subdivide the NC5C and NC5E subzones, respectively, at least at a regional scale.

The lowermost sample from the Barranco de Cavila section already contains *F. oblongus*. Samples from the top of the section contain *Hayesites irregularis* and *Conusphaera rothii*. The FO of *H. irregularis* with nearly circular (equidimensional) outline, similar to the holotype (Roth and Thierstein, 1972) and hypotypes (Thierstein, 1973), was recorded from the upper part of this section (sample X.Kv2-644, 46.1 m). Cross-polarized micrographs of these specimens, together with scaled reproductions of the holotype and hypotype are shown in Figs. 4A–H. However, scarce specimens similar to this species, but having an elongated outline and poorly defined elements (named here morphotype E; Figs. 4I–L) were recorded from well below, in stratigraphic levels equivalent to the uppermost part of the Feraudianus Subzone of ammonites (sample X.Kv2-576, 41.4 m). The specimens of *H. irregularis* morphotype E coexist with those of circular outline (true *H. irregularis*) across most of the Sarasini Zone. As the FO of *H. irregularis* is an important datum, used to define the boundary between NC5 and NC6 nannofossil zones (Bralower et al., 1995), we tentatively opted for the use of the FO of *H. irregularis* s.l. (early morphotype E) as zonal marker. According to this, most of the Barranco de Cavila section (from its base to 41.4 m) was assigned to NC5E Subzone, while its uppermost part (41.4 m to its top) was assigned to the NC6A Subzone (Bralower et al., 1985). Subzones NC5E (*p.p.*) and NC6A (*p.p.*) were then identified across the Barranco de Cavila section (Fig. 3).

The successive FOs of *Lithraphidites* sp. cf. *L. magnus* (sample X.Kv2-155, 11.7 m; Fig. 2N) and *Micrantholithus stellatus* (sample X.Kv2-454, 32.7 m) have shown stratigraphic potential at the basin scale (Aguado et al., 2017; pers. observations) and could be used to subdivide the NC5E Subzone (Fig. 2). In particular, the FO of *Lithraphidites* sp. cf. *L.*

*magnus* is used here as an alternative correlation event to determine the overlap between the Arroyo Gilico and Barranco de Cavila sections. The FO of *Lithraphidites magnus* was recorded from the uppermost part of the Feraudianus Subzone (sample X.Kv2-580, 41.7 m; Fig. 2M). *L. magnus* was previously described as a subspecies (*L. alatus* ssp. *magnus*) from the DSDP 603 by Covington and Wise (1987). The sporadic record of specimens of *Calcicalathina oblongata*, *Cruciellipsis cuvillieri*, *Rucinolithus wisei* and *Diadorhombus rectus* indicates some reworking from the Valanginian–Hauterivian rocks into the marlstones of the Barranco de Cavila section.

## 5. Results of magnetic susceptibility and carbonate calcium contents

### 5.1 Arroyo Gilico section

In the Arroyo Gilico section,  $\text{CaCO}_3$  content ranges from 11.3 % to 98.0 %, while mass-specific magnetic susceptibility (MS) ranges from  $7.9 \times 10^{-9} \text{ m}^3 \cdot \text{kg}^{-1}$  to  $74.9 \times 10^{-9} \text{ m}^3 \cdot \text{kg}^{-1}$  (Fig. 2).  $\text{CaCO}_3$  and MS show an excellent inverse, linear correlation (Fig. 5), with a correlation coefficient of 0.87. The intercept value of the best-fit linear regression ( $86.4 \times 10^{-9} \text{ m}^3 \cdot \text{kg}^{-1}$ ) is near the mass-specific values of the illite and smectite (100 to  $150 \times 10^{-9} \text{ m}^3 \cdot \text{kg}^{-1}$ ; Hunt et al., 1995), which are dominant within the clay mineral assemblages (Moiroud et al., 2012). These results imply that paramagnetic clay minerals control the MS values, while the ratio between carbonate and detrital supply control the fluctuations of the MS series, as this is the case in the Río Argos section (Martinez, 2018).

The long-term trend of the MS and  $\text{CaCO}_3$  series (red curve) were calculated applying a LOWESS coefficient of 0.25. At large scale, the average MS values decrease from the Krenkeli Subzone to the Mortilleti Subzone, increase from the Picteti Subzone to the Nicklesi

Zone, decrease in the Pulchella and Compressissima Zones and increase in the Moutonianum and Vandenheckii Zones (Fig. 2).

### 5.2. Barranco de Cavila section

In the Barranco de Cavila section, the  $\text{CaCO}_3$  values range from 23.8 to 100 %, while mass-specific MS values range from  $6.9 \times 10^{-9} \text{ m}^3 \cdot \text{kg}^{-1}$  to  $79.2 \times 10^{-9} \text{ m}^3 \cdot \text{kg}^{-1}$  (Fig. 3). As in the Arroyo Gilico section, MS and  $\text{CaCO}_3$  are strongly inversely correlated ( $r = -0.91$ ; Fig. 5). The intercept value of the best-fit linear regression ( $95.3 \times 10^{-9} \text{ m}^3 \cdot \text{kg}^{-1}$ ) suggests that the MS values are carried by paramagnetic clay minerals while their fluctuations are governed by dilution from  $\text{CaCO}_3$  content.

In the interval from 0.50 to 21.30 m (Fig. 5), the MS series has an average value of  $22.4 \times 10^{-9} \text{ m}^3 \cdot \text{kg}^{-1}$  and a variance of  $8.07 \times 10^{-17} \text{ m}^6 \cdot \text{kg}^{-2}$ . In this interval, the  $\text{CaCO}_3$  content has an average value of 79.9 % and a variance of 120 %<sup>2</sup>. In the interval from 21.30 m to 68.06 m (Fig. 3), the MS values increase to an average value of  $33.4 \times 10^{-9} \text{ m}^3 \cdot \text{kg}^{-1}$  and a variance of  $2.22 \times 10^{-16} \text{ m}^6 \cdot \text{kg}^{-2}$ . In this interval, the average  $\text{CaCO}_3$  content decreases to 67.5 % and the variance increases to 232 %<sup>2</sup>. Thus, from 21.30 m upward, the clay content in the sediment increases and both MS and  $\text{CaCO}_3$  content show higher-amplitude fluctuations than below (Fig. 3). For the purpose of spectral analyses, this section was separated into two intervals, from the base of the series to 21.30 m, and from 15 m to the top of the series. The lower interval thus encompasses the Vandenheckii Zone and the base of the Sartousiana Zone, while the upper interval encompasses the whole of the Sartousiana Zone to the earliest Aptian. The trends of both intervals were calculated using best-fit linear regressions.

## 6. Spectral analyses

### 6.1. Arroyo Gilico

The  $2\pi$ -MTM spectra performed on the MS and  $\text{CaCO}_3$  series of Arroyo Gilico shows significant periods ( $> 95\%$  CL) ranging from 11 m to 0.37 m (Figs. 6A, B). Additional periods are observed at 6.8 m, 2.1 m and 1.4 m below the 95 % CL.

The Arroyo Gilico section covers 74.68 m and a duration of 4.02 Myr based on previous duration assessments of ammonite zones and subzones from astrochronology and bed counting (Bodin et al., 2006a; Martinez et al., 2012, 2013; Aguirre-Urreta et al., 2019). It represents a mean sedimentation rate of  $1.85 \text{ cm.kyr}^{-1}$ . The COCO method was thus applied on a range of sedimentation rates from 0.7 to  $6 \text{ cm.kyr}^{-1}$  to ensure all reasonable sedimentation rates are covered. The COCO analysis of the whole Arroyo Gilico series shows the highest significant correlation ( $p\text{-value} < 1 \times 10^{-3}$ ) at sedimentation rates of  $0.82 \text{ cm.kyr}^{-1}$ ,  $1.29 \text{ cm.kyr}^{-1}$ ,  $1.71 \text{ cm.kyr}^{-1}$ ,  $2.69 \text{ cm.kyr}^{-1}$  (Figs. 6C, D). Other increases in correlation coefficients are found at sedimentation rates of  $2.1\text{-}2.2 \text{ cm.kyr}^{-1}$  and  $3.5 \text{ cm.kyr}^{-1}$  in the MS data.

The spectrogram performed on 30-m width windows (Fig. 7A) shows a period increasing from 5 to 7.3 m from levels 0 to 30 m. In this interval, the dominant periods are at 3.3 and 2.1 m. Still in the 0-30 m interval, shorter periods can be observed at 1.4, 1.1, 0.79, 0.67 m and from 0.63 to 0.43 m (Fig. 7B). From levels 35 to 65 m, a period at 11 m appears and reaches a maximum in amplitude from 40 to 60 m (Fig. 7A). In this interval, periods at  $\sim 3$  and  $\sim 2$  m can still be observed with lower amplitudes compared to the lower interval. Shorter periods can be observed at 1.7, 1.2, 0.80 and 0.64 m from level 25 to 45 m, and at 3.1, 1.0, 0.72 and 0.58 m from level 45 to 65 m (Fig. 7B). From 65 m to the top of the series, the peak at 11 m decreases in amplitude and a peak at 5.8 m appears (Fig. 7A). In addition, periods at

$\sim 3$  and  $\sim 2$  m are not observed anymore. Instead, periods at 1.6 m, 0.83 m and from 0.58 to 0.42 m are observed (Fig. 7B).

The eCOCO analysis shows significant correlation between the spectra of the sedimentary and astronomical series at sedimentation rates of 0.83, 1.10, 1.3-1.4 and 1.68  $\text{cm.kyr}^{-1}$  from levels 0 to 40 m (Fig. 7C); at sedimentation rates of 1.11 and around 2.3  $\text{cm.kyr}^{-1}$  from level 40 to 60 m; and of 0.90, 1.27, 1.7-1.8 and 2.14  $\text{cm.kyr}^{-1}$  from level 60 m to the top of the series.

From the spectrograms and the eCOCO diagram, the series was divided into three intervals: (i) Interval 1 from 0 to 40 m, Interval 2 from 39 to 60 m and Interval 3 from 60 m to the top of the series. Interval 1 encompasses the upper part of the Balearis Zone to the lower part of the Nicklesi Zone. The lithology in Interval 1 can be correlated to the Río Argos section, calibrated by astrochronology (Marín et al., 2012, 2015). Interval 2 encompasses the upper part of the Hugii Zone to the base of the Vandenheckii Zone. This interval can be notably correlated to the Angles section, calibrated by astrochronology (Bodin et al., 2006a). Interval 3 encompasses the end of the Moutonianum Zone to the Vandenheckii Zone *p.p.* This interval is notably recovered in the Barranco de Cavila section, allowing intercomparison of astrochronologic frameworks. In each of the intervals, a  $2\pi$ -MTM spectrum was performed to obtain a synthetic overview of the cycles recorded and a COCO analysis was applied to estimate the best sedimentation rates from fitting the spectra to the spectrum of the astronomical solutions.

In Interval 1, the  $2\pi$ -MTM spectra of the MS and  $\text{CaCO}_3$  series show a group of significant spectral peaks ( $> 95$  % CL) from 2.0 to 1.2 m, at 0.80 m and from 0.63 to 0.41 m (Figs. 6M, N). In addition, spectral peaks are observed in lower frequencies at 5.7-6.7 m and 3.3 m. The COCO analysis shows highest correlations ( $p$ -value  $< 1 \times 10^{-2}$ ) at sedimentation rates of 0.85  $\text{cm.kyr}^{-1}$ , from 1.08 to 1.43  $\text{cm.kyr}^{-1}$  and at 1.70  $\text{cm.kyr}^{-1}$  (Figs. 6O, P). Other

increase in the significance level occur at sedimentation rates of 2.66 cm.kyr<sup>-1</sup> and 3.53 cm.kyr<sup>-1</sup>.

In Interval 2, the  $2\pi$ -MTM spectra show significant spectral peaks (> 95 % CL) at 10 m, 2.7 m, and from 1.1 to 0.42 m (Fig. 6I, J). Additional peaks appear with low amplitudes at 1.6, 1.3 and 0.38 m. The COCO analysis displays the highest correlations ( $p$ -value <  $1 \times 10^{-2}$ ) at mean sedimentation rates of 0.83 cm.kyr<sup>-1</sup>, 2.14 cm.kyr<sup>-1</sup> and 2.64 cm.kyr<sup>-1</sup> (Figs. 6K, L). Additional significant increase in sedimentation rate is observed at 0.99 cm.kyr<sup>-1</sup>.

In Interval 3, the  $2\pi$ -MTM spectrum of the MS series shows a double peak in low frequencies at 9.9 m and 5.9 m, other peaks at 1.6 m, 1.1 m, 0.77 m, and from 0.59 m to 0.25 m (Fig. 6E, F). The COCO analysis displays significant correlations ( $p$ -value <  $5 \times 10^{-2}$ ) at mean sedimentation rates of 0.89 cm.kyr<sup>-1</sup> and 1.25 cm.kyr<sup>-1</sup> (Figs. 6G, H). An additional increase in sedimentation rate is observed at 1.62 cm.kyr<sup>-1</sup>.

## 6.2. Barranco de Cavila

The spectral analyses of the Barranco de Cavila section were performed on two intervals of the series, following the change in the mean values and amplitudes of changes described in section 5.2. Interval 4 covers from 0 to 21.30 m, which corresponds to the Vandenheckii and the beginning of the Sartousiana zones. Interval 5 covers from 21.30 m to the top of the series, from the Sartousiana to the Forbesi zones.

### 6.2.1. Interval 4

In Interval 4, significant spectral peaks (> 95 % CL) are observed at 2.9 m, 1.0 m, 0.54 m, 0.44 m, 0.37 m and 0.31 m (Figs. 8M, N). Additional peaks are observed at 1.5 m and 0.75 m. The COCO analysis was performed on both the MS and the CaCO<sub>3</sub> series. The duration of

the Vandenheckii Zone was estimated as 0.8 Myr from a previous cyclostratigraphic assessment (Bodin et al., 2006a). Considering that the thickness of this zone in Barranco de Cavila is at least 16 m, it represents a minimum sedimentation rate of  $2 \text{ cm.kyr}^{-1}$ . The sedimentation rates tested with the COCO method thus ranges from 0.7 to  $6 \text{ cm.kyr}^{-1}$  to ensure all reasonable sedimentation rates have been tested. The COCO analysis indicates significant correlations between the spectra of the sedimentation series and the astronomical solutions at sedimentation rates of 0.84, 1.16 and  $2.45 \text{ cm.kyr}^{-1}$  (Figs. 8O, P).

The spectrogram performed on 15-m width windows (Fig. 9A) shows a period ranging from  $\sim 12 \text{ m}$  to  $7.3 \text{ m}$  from level 7 m to the top of Interval 4. A period at  $\sim 3 \text{ m}$  is observed throughout the interval while a period at  $1.6 \text{ m}$  is observed in the lowermost 10 m. In the spectrogram performed on 7-m width windows (Fig. 9B), the period of  $\sim 3 \text{ m}$  is observed from level 3 m to 9 m and from level 15 m to 21 m, while the period at  $1.6 \text{ m}$  is observed from level 9 to 14 m. The discrepancy in the intervals where the periods are observed is due to the selection of the window size. In the 15-m spectrogram, the windows encompass more than half of the length of Interval 4, which favours accuracy in the detection of low frequencies at the cost of their precise stratigraphic location. The 7-m spectrogram is much suitable to detect the location of the change in the dominant periods in the signal. Other periods are observed at 1.1, 0.64, 0.32 and  $0.27 \text{ m}$  in the lowermost part of Interval 4. Periods at 0.90, 0.74, 0.54 and  $0.45 \text{ m}$  are observed in the middle part of Interval 4 and a period at  $0.97 \text{ m}$  is observed in the upper part of Interval 4.

The eCOCO analysis shows significant correlations at a sedimentation rate of 0.85-0.86  $\text{cm.kyr}^{-1}$  from levels 0 to 9 m and from level 15 m to the top of the interval. A sedimentation rate of  $1.17 \text{ cm.kyr}^{-1}$  is observed from levels 4 to 11 m, a sedimentation rate of  $1.11 \text{ cm.kyr}^{-1}$  from 15 m to the top of the interval. Sedimentation rates around  $2.6\text{-}2.8 \text{ cm.kyr}^{-1}$  from levels 2 to 7 m and from 16 m to the top of Interval 4 (Fig. 9C).

### 6.2.2. Interval 5

In Interval 5, significant spectral peaks ( $> 95\%$  CL) are observed at 21 m, 8.8 m, 4.3 m, 2.7 m, 1.7 m, 1.1 m, 0.76 m, 0.52 m and 0.43 m (Figs. 8A, B). The COCO analysis was performed on both the MS and the  $\text{CaCO}_3$  series. The duration of the Sartousiana to the Sarasini Zone was estimated as 1.68 Myr from a previous cyclostratigraphic assessment (Bodin et al., 2006a). Considering the thickness of this interval is 39.5 m in Barranco de Cavila, it represents a sedimentation rate of  $2.35 \text{ cm.kyr}^{-1}$ . The sedimentation rates tested with the COCO method thus ranges from 0.7 to  $7 \text{ cm.kyr}^{-1}$  to ensure all reasonable sedimentation rates have been tested. The COCO analysis indicates highest correlations ( $p\text{-value} < 1 \times 10^{-3}$ ) at mean sedimentation rates of 1.22 and  $3.98 \text{ cm.kyr}^{-1}$  (Figs. 8C, D). Additional significant correlations are observed at 0.90, 1.71, 2.06, 3.10,  $5.14 \text{ cm.kyr}^{-1}$ .

The spectrogram performed on 40-m width windows (Fig. 10A) shows a peak at 21 m at level 20 m, whose period decreases to 12 m at level 40 m and increases to 20 m at the top of the series. Additional periods are observed at 8.5 m and 4.8 m (from levels 40 to 60 m), at 3.6 m (from levels 20 to 45 m) and 2.7 m on average (from 15 to 35 m and from 50 m to the top of the series).

The spectrogram performed on 15-m width windows (Fig. 10B) shows from level 15 m to 40 m a peak at 2.6 m, whose period increases to 3.8 m, a peak at 1.0 m and a peak at 0.52 m. Other peaks with lower amplitudes are observed at 0.44 m and 0.37 m. From 40 m to the top of the series, peaks are observed at 5.0 m and 1.7 m. Other peaks are locally observed at 0.75 m (from levels 45 to 55 m), 1.2 m (from levels 50 to 60 m), and 2.9 m, 0.61 m, 0.50 m, and 0.45 m (from 60 m to the top of the series).

The eCOCO analysis shows significant correlations at a sedimentation rate around 2.7 cm.kyr<sup>-1</sup> from levels 15 to 30 m, 0.88 cm.kyr<sup>-1</sup> from levels 25 to 40 m, 4.04 cm.kyr<sup>-1</sup> from levels 30 to 50 m, 1.24 cm.kyr<sup>-1</sup> from level 40 m to the top of the series and 1.70 cm.kyr<sup>-1</sup> from levels 45 m to the top of the series (Fig. 10C). From the spectrograms and the eCOCO analysis, Interval 5 can be subdivided into two subintervals. Interval 5a, from 15 to 45 m, encompasses the Sartousiana Zone. The highest coefficient correlations ( $p$ -value  $< 1 \times 10^{-3}$ ) are observed at sedimentation rates of 0.92 cm.kyr<sup>-1</sup> and 4.09 cm.kyr<sup>-1</sup> (Figs. 8 K, L). In addition, a significant coefficient correlation is observed at a sedimentation rate of 2.97 cm.kyr<sup>-1</sup>. The  $2\pi$ -MTM spectra of the MS series shows significant periods ( $> 95\%$  CL) at 15 m, 4.1 m, 2.5 m, 1.0 m, 0.51 m, 0.44 m and 0.37 m (Figs. 8I, J).

Interval 5b, from 40 m to the top of the series, encompasses the Giraudi to the Forbesi zones. The highest coefficient correlations ( $p$ -values  $< 1 \times 10^{-2}$ ) are observed at sedimentation rates of 1.24 and 1.73 cm.kyr<sup>-1</sup> (Figs. 8G, H). An additional significant coefficient correlation is observed at sedimentation rate of 4.26 cm.kyr<sup>-1</sup>. The  $2\pi$ -MTM spectrum of the MS series shows significant periods ( $> 95\%$  CL) at 7.0 m, 1.7 m, 1.1 m, 0.75 m, 0.61 m and 0.44 m (Figs. 8E, F).

## 7. Discussion

### 7.1. Interpretation of the sedimentary cycles

#### 7.1.1. Interval 1: Arroyo Gilico, Balearis to Hugii zones

Interval 1, the COCO analysis shows significant sedimentation rates ranging from 0.85 cm.kyr<sup>-1</sup> to 1.71 cm.kyr<sup>-1</sup> (Figs. 6O, 6P, 7C). The interval from the Krenkeli Subzone to the Hugii Zone (Interval 1) in Arroyo Gilico is correlated to the Río Argos section through ammonite zonation and bed pattern (Company et al., 2003a). The Río Argos section has also

been calibrated with astrochronology (Martinez et al., 2012, 2015; Aguirre-Urreta et al., 2019), which offers the opportunity to correlate the eccentricity cycle to the Arroyo Gilico section. The interval from the Krenkeli Subzone to the Hugii Zone covers a duration of 1.68 Myr (Aguirre-Urreta et al., 2019) and has a thickness of 36.6 m in Arroyo Gilico, which represents a mean sedimentation rate of  $2.18 \text{ cm.kyr}^{-1}$ . According to this time scale, this mean sedimentation rate is assessed at  $3.27 \text{ cm.kyr}^{-1}$  in the Balearis *p.p.* Zone,  $1.08 \text{ cm.kyr}^{-1}$  in the Ohmi Subzone,  $1.78 \text{ cm.kyr}^{-1}$  in the remaining of the Ohmi Zone and  $2.08 \text{ cm.kyr}^{-1}$  in the Hugii Zone. These estimates reflect the short-term variations in the sedimentation rate in Interval 1 and a condensation in the Ohmi Subzone. The sedimentation rate of  $1.71 \text{ cm.kyr}^{-1}$  shown in the COCO analysis appears the most likely from the Mortilleti to the Colombiana subzones.

In the Balearis *p.p.* Zone, main periods are observed at 3.5 m, 2.0 m, 1.1 m and 0.67 m (Figs. 7A, B). According to the eCOCO analysis, the most likely sedimentation rate in this interval would be  $1.10 \text{ cm.kyr}^{-1}$  (Fig. 7C), implying (i) the 3.3-m and 1.1-m cycles respectively fall into the band of the 405-kyr and 100-kyr eccentricity cycles and (ii) a duration of at least 1.2 Myr for the Krenkeli and Angulicostata subzones. This is much higher than previous cyclostratigraphic-derived durations in Tethys and in the Río Argos section (Bodin et al., 2006a; Martinez et al., 2015). Instead, with a mean sedimentation rate of  $3.27 \text{ cm.kyr}^{-1}$ , the 3.3-m falls into the band of the 100-kyr eccentricity, the 1.1-m peak in the obliquity, and the 0.67-m peak in the precession. This solution appears more consistent with previous cyclostratigraphic-derived durations of this time interval.

The interval from the Mortilleti to the Colombiana subzones show periods from 6.2 to 7.3 m, from 2.0 to 1.7 m, from 1.4 to 1.2 m, at 0.80 m and from 0.63 to 0.43 m (Fig. 7C). Assuming a sedimentation rate ranging from  $1.78$  to  $2.08 \text{ cm.kyr}^{-1}$ , the peaks from 7.3 to 6.2 m fall into the band of the 405-kyr eccentricity, the peaks from 2.0 to 1.7 m into the band of the 100-kyr

eccentricity, the peaks from 0.80 to 0.64 m into the obliquity and the peaks from 0.56 to 0.43 m to the precession.

The filter of the 405-kyr eccentricity band at Arroyo Gilico correlates with the 405-kyr band identified at Río Argos from the Angulicostata Subzone to the Hugii Zone (Fig. 11). Maxima of the 405-kyr cycle in both sections are found within the last 100-kyr cycle below the boundary between the Angulicostatus and Ohmi subzones, at the boundary between the Mortilleti and the Picteti subzones, within the last 100-kyr cycle below the Hauterivian-Barremian boundary and just below the FO of *M. spinuler tun*. Below the Angulicostatus Subzone, two maxima of the filter of the 405-kyr band are observed in the Krenkeli Subzone do not correlate with the filter of the 405-kyr band at Río Argos. In this interval, the thickness of the longest period decreases in Arroyo Gilico and does not fall anymore within the band of the 405-kyr cycle. The base of cycle H11 shown in Arroyo Gilico thus corresponds to the base of this cycle identified in the Río Argos section (Fig. 11).

The filter of the 100-kyr eccentricity band correlates with the Río Argos section with three noticeable exceptions. The Angulicostatus Subzone contains two short eccentricity cycles at Arroyo Gilico vs. one at Río Argos; the Ohmi Subzone is so condensed that no short-eccentricity cycle is recorded; a short-eccentricity cycle is missing in the Picteti Subzone (cycles 30 and 31, Fig. 11), reflecting a short-term hiatus. In addition, cycle 22 in the Krenkeli Subzone and 37 in the Colombiana Subzone contain two local maxima and seem to be double. In cycles 22 and 37, one of the double peaks only covers one marl-limestone alternation and one obliquity cycle. These double peaks correlate to one 100-kyr eccentricity cycles in the Río Argos section. Cycle 22 as we sequence here contains 3 obliquity and 6 precession cycles while cycle 37 contain 2.5 obliquity and 5 precession cycles, which correspond to the hierarchy between the 100-kyr eccentricity, the obliquity and the precession cycles.

### 7.1.2. Interval 2: Arroyo Gilico, Hugii to Moutonianum zones

Interval 2 covers the Colombiana Subzone to the Moutonianum Zone (Fig. 12). The COCO analysis indicates two highest significant sedimentation rates at  $0.83 \text{ cm.kyr}^{-1}$  and  $2.64 \text{ cm.kyr}^{-1}$  (Fig. 6K, L). If the hypothesis of a sedimentation rate of  $0.83 \text{ cm.kyr}^{-1}$  is retained, the duration of the interval from the Nicklesi to the Moutonianum Zone would be  $\sim 3.0 \text{ Myr}$ , while this duration would be  $\sim 1.0 \text{ Myr}$  if the hypothesis of a sedimentation rate of  $2.64 \text{ cm.kyr}^{-1}$  is retained. In the Angles section, the duration of this interval was estimated as  $1.54 \text{ Myr}$ , based on cycle counting (Bodin et al., 2006a). This is in closer agreement with the hypothesis at  $2.64 \text{ cm.kyr}^{-1}$ . In that case, the band of the 405-kyr eccentricity would correspond to the peak at  $10 \text{ m}$ ; the band of the 100-kyr eccentricity to the peak at  $2.7 \text{ m}$ ; the band of obliquity to the peak of  $1.1 \text{ m}$  and the band of the precession cycle would range from  $0.65$  to  $0.42 \text{ m}$ . The peaks at  $1.7$  and  $0.8 \text{ m}$  notably appear in the Nicklesi Zone, where the short-eccentricity cycle has a thickness of  $3.5 \text{ m}$  (Fig. 7). These cycles could thus be attributed to the obliquity and the precession cycles, respectively. The peak at  $0.7 \text{ m}$  appears in the Compressissima and Moutanianum zones, where the short-eccentricity cycle has thicknesses ranging from  $4.3$  to  $2.5 \text{ m}$ , with an average of  $3.1 \text{ m}$  (Fig. 7). The peak at  $0.7 \text{ m}$  is thus attributed to the precession cycle.

### 7.1.3. Interval 3: Arroyo Gilico, Vandenheckii Zone

In Interval 3, the COCO analysis indicates three highest significant sedimentation rates at  $0.89 \text{ cm.kyr}^{-1}$ ,  $1.25 \text{ cm.kyr}^{-1}$  and  $1.69 \text{ cm.kyr}^{-1}$  (Figs. 6G, H), leading to a duration of the Vandenheckii (*p.p.*) Zone at  $1.4 \text{ Myr}$ ,  $0.98 \text{ Myr}$  and  $0.74 \text{ Myr}$ , respectively. In the Angles section, the duration of the Vandenheckii Zone was estimated as  $0.8 \text{ Myr}$  from bed counting (Bodin et al., 2006a). This duration is more consistent with the sedimentation rates of  $1.25$

and  $1.69 \text{ cm.kyr}^{-1}$ . In both cases, the peaks of 6 m and 1.6 m fall into the band of the 405-kyr and 100-kyr eccentricity, respectively. The peaks of 0.80 m and 0.59 m fall into the band of the obliquity cycles, while the peaks from 0.47 to 0.25 m respectively fall into the band of the precession.

#### 7.1.4. Interval 4: Barranco de Cavila, Vandenheckii Zone

In Interval 4 in the Barranco de Cavila section, the COCO analysis indicates significant sedimentation rates at 0.84, 1.17 and  $2.45 \text{ cm.kyr}^{-1}$  (Figs. 8G, H). Accounting for the estimated duration of the Vandenheckii Zone at Angeles and the thickness of this zone (*p.p.*) in Barranco de Cavila, the estimated mean sedimentation rate would be  $\sim 2 \text{ cm.kyr}^{-1}$ , in between the significant sedimentation rates at 1.17 and  $2.45 \text{ cm.kyr}^{-1}$ . The spectrogram performed on 7-m width windows reveals a peak at 3 m, from 0 to 10 m and from 15 to 20 m (Fig. 9D), which falls into the band of the 100-kyr eccentricity if the hypothesis of a sedimentation rate of  $2.45 \text{ cm.kyr}^{-1}$  is retained. In the interval from 10 to 15 m, a peak at 1.5 m is recorded instead and could fall into the band the 100-kyr cycle if the hypothesis of a sedimentation rate of  $1.17 \text{ cm.kyr}^{-1}$  is retained. The eCOCO analysis follows this trend showing significant coefficient correlations at sedimentation rates around  $2.7 \text{ cm.kyr}^{-1}$  in the lower and upper part of Interval 4, while the middle of the interval shows a maximum of correlation coefficient at a sedimentation rate of  $1.17 \text{ cm.kyr}^{-1}$  (Fig. 9C). The filter of the whole band from the 3-m to the 1.5-m peaks shows 8 cycles in the Vandenheckii (*p.p.*) Zone (Fig. 13). In addition, the filter of the peak at 5 to 7 m and the amplitude modulation of the band from 3 to 1.5 m shows a cycle covering 3 to 4 short-eccentricity, which fits in the expression of a 405-kyr eccentricity cycle. Thus, this interval shows a sedimentation of  $\sim 2.7 \text{ cm.kyr}^{-1}$  in its lower and upper part, and a decrease sedimentation to  $\sim 1.2 \text{ cm.kyr}^{-1}$  in its middle part.

### 7.1.5. Interval 5: Barranco de Cavila, Sartousiana to Forbesi zones

In Interval 5 in the Barranco de Cavila section (from level 15 m to the top of the series), the highest significant sedimentation rates are observed at 1.22 and 3.98  $\text{cm.kyr}^{-1}$  (Figs. 8C, D). Additional significant sedimentation rates are observed at 0.90, 1.71, 2.08, 3.10 and 5.14  $\text{cm.kyr}^{-1}$ . As in other intervals showing several significant sedimentation rates, this could reflect high-frequency variations in the sedimentation rate through this interval. In Interval 5a (15 to 45 m), significant correlations are observed at sedimentation rates of 0.92, 2.97 and 4.09  $\text{cm.kyr}^{-1}$  (Fig. 8K, L). The duration of the Sartousiana Zone was estimated as 0.8 Myr in Bodin et al. (2006a), implying a mean sedimentation rate of Interval 5a of 3.52  $\text{cm.kyr}^{-1}$ , in between the sedimentation rates of 2.97 and 4.09  $\text{cm.kyr}^{-1}$ . The eCOCO analysis shows a likely sedimentation rate of  $\sim 2.7$   $\text{cm.kyr}^{-1}$  from 15 to 30 m increasing to 4.0-4.1  $\text{cm.kyr}^{-1}$  from 30 to 40 m (Fig. 10C). The spectrograms realized on Interval 5 shows a period of 2.6 m expressed from 15 to 25 m, which increases to 3.8 m from 27 to 40 m (Fig. 10B). This period then represents the 100-kyr eccentricity cycle. The peak of 1.0 m observed in the lower part of Interval 5a (Fig. 10B) represents the obliquity cycle and falls into the band precession from 30 m upward when the sedimentation increases. The peak of 0.5 m represents the precession cycle from 15 to 30 m and falls into sub-precession bands from 30 m upward when the sedimentation increases. The 12-m cycle corresponds to the 405-kyr eccentricity cycle. In the lower part of Interval 5a, the 20-m peak is too long to represent the 405-kyr cycle. In this part of Interval 5a, the rapid increase in MS values and decrease in  $\text{CaCO}_3$  content due to change in the mode of sedimentation to detrital dominated marl-limestone alternations may have altered the sedimentary expression of the 405-kyr cycle. In the lower part of the Sartousiana Zone, the 405-kyr eccentricity cycle is bounded using the bandpass filter of this band from Interval 4, i.e. before the rapid change in lithology (Fig. 13).

In Interval 5b (40 m to the top), significant correlations are observed at sedimentation rates of 1.24, 1.73, 4.20 cm.kyr<sup>-1</sup> (Figs. 8G, H). In the Angles section, the duration of the interval from the Giraudi Zone to the Oglanlensis Zone was estimated from bed counting as *ca.* 1.22 Myr (Bodin et al., 2006a), which corresponds to a mean sedimentation rate of 1.8 cm.kyr<sup>-1</sup>, ranging from 0.98 cm.kyr<sup>-1</sup> in the Giraudi Zone to 2.9 cm.kyr<sup>-1</sup> in the Sarasini Zone. In the eCOCO analysis, the interval from 40 to 55 m in Barranco de Cavila (Giraudi and Sarasini zones) shows highest correlations at a sedimentation rate of 1.24 cm.kyr<sup>-1</sup> and at 1.70 cm.kyr<sup>-1</sup> from 55 m to the top of the series (Oglanlensis Zone) (Fig. 10C). Thus, in the spectra (Figs. 8E, F), the peak of 7.0 m is attributed to the 405-kyr eccentricity cycle, the peak of 1.7 m to the 100-kyr eccentricity cycle and the peak of 0.44 m to the precession cycle. The peak of 0.61 m is expressed from level 60 m to the top of the series while the peak of 1.7 m disappears and a peak at 2.9 m appears. This peak of 0.61 m is attributed to the precession cycle and the peak of 2.9 m to the 100-kyr eccentricity cycle. The peak of 1.1 m is expressed from 50 to 60 m and is attributed to the obliquity cycle.

The bandpass filters of the 100-kyr eccentricity band leads to approx. ten 100-kyr eccentricity cycles in the Sartousiana Zone, corresponding to a duration of ~1.0 Myr (Fig. 14), which agrees with the bed counting in the Angles section (Bodin et al., 2006a). The filter of the 405-kyr eccentricity band indicates a maximum of the filter at cycle 61 and 65 (Fig. 14). Spectral analyses in Interval 4 shown that the 405-kyr eccentricity has a maximum at cycle 57 (Fig. 13), which implies that the Sartousiana Zone shows two complete 405-kyr cycles plus an incomplete one at the top of the zone, in agreement with the duration of the zone obtained from the Angles section. In the Giraudi and Sarasini zones, the thicknesses of the 405-kyr eccentricity cycles decrease compared to the B8 cycle at 7.47 m (B9 cycle), 8.48 m (B10 cycle) and 8.60 m (B/A cycle) (Fig. 14) in agreement with the 40-m spectrogram and the eCOCO analysis (Fig. 10). In Interval 5b, the boundaries of the 405-kyr eccentricity cycles

are positioned within cycle 70 and within cycle 74 (Fig. 14). In summary, the 405-kyr eccentricity cycle covers four to five 100-kyr eccentricity cycles. From the record of the 405-kyr eccentricity cycles, the duration of the interval from the Sartousiana to the Sarasini Zone is proposed at 1.82 Myr, in line with the 1.68 Myr calculated in the Angles section (Bodin et al., 2006a).

### 7.2. A revised timescale of the Barremian Stage

The Barremian Stage is sequenced from the filters of the identified 405-kyr eccentricity band in the various proxies. The cycles boundaries are positioned at the average position of the filters of the various proxies from the sections studies here and Río Argos (Figs. 11-14, see also Supplement 1). A total of ten complete 405-kyr eccentricity cycles are observed plus incomplete cycles at the bottom and the top of the Barremian Stage. Assuming a constant sedimentation rate within each of the 405-kyr eccentricity cycles, this leads to a duration of the Barremian Stage of 4.18 Myr. This duration is anchored to the age of the base of the Krenkeli Subzone calculated at  $127.22 \pm 0.19$  Ma from integrated radio-astrochronology between the Neuquén Basin and the Tethyan area (Aguirre-Urreta et al., 2019). The obtained age of the base and the top of the Barremian Stage are  $125.98 \pm 0.21$  Ma and  $121.40 \pm 0.34$  Ma, respectively. The age uncertainties include the age of the Krenkeli Subzone ( $\pm 0.19$  Ma), the uncertainty in the astrochronological age model (detailed below) and the uncertainty of the position of the top of the Barremian Stage (+ 0.02 Ma / - 0.25 Ma).

The uncertainty of the astrochronological age model is calculated using the Bchron approach (Haslett and Parnell, 2008). The R-package uses a compound Poisson-gamma law to ensure realistic randomised ages following a monotonous function (i.e., higher levels correspond to younger ages). The Poisson-gamma law also ensures that levels further from an

anchor point have higher age uncertainties than levels close to an anchor point. The model was initially applied to calculate the ages between tuff horizons and needs the uncertainty of the dating and the thickness of the horizons. In this case study, the dating uncertainty corresponds to the uncertainty in the period of the 405-kyr eccentricity cycle (1.3 kyr; Laskar et al., 2004). The positions of the boundary of the 405-kyr cycles differ from a proxy to another and from a section to another, so that each boundary is defined with an uncertainty interval, that we assimilate here to the horizon thickness (Figs. 11-14, see also Supplement 1). The age uncertainty at the base of the Barremian Stage is 0.09 Myr ( $2\sigma$ ) and is 0.12 Myr ( $2\sigma$ ) at the top of the Barremian Stage (Fig. 15). An additional uncertainty of (+0.02 Myr / -0.25 Myr) is added at the top of the Barremian Stage due to the uncertainty of the position of the base of the Oglanlensis Zone. The upper uncertainty in the duration of the Barremian Stage is  $\sqrt{0.09^2 + 0.12^2 + 0.02^2} = 0.15$  Myr, while the lower uncertainty is  $\sqrt{0.09^2 + 0.12^2 + 0.25^2} = 0.29$  Myr. The total duration of the Barremian Stage is thus assessed at  $4.58^{+0.15}_{-0.29}$  Myr.

The analysis done here allows the tuning of the Barremian Stage and its biostratigraphic subdivisions to the eccentricity cycles. It is worth noting that the duration of the Barremian Stage assessed here agrees with the estimates from the Umbria-Marche Basin (~4.4 Myr; Sprovieri et al., 2006) and the Vocontian Basin (4.52 Myr; Bodin et al., 2006). As mentioned above, short-term hiatuses and variations in the sedimentation rate may have impacted the interpretations, which increased the uncertainty of the duration estimated to ~0.3 Myr. Similar studies performed in Angles or other sections well dated by ammonites should allow to verify or precise the anchoring of the eccentricity cycles to biostratigraphic subdivisions, as we successfully did here between the Arroyo Gilico and the Río Argos sections (Fig. 11). From this correlation, the duration of the Ohmi Subzone, condensed in the Arroyo Gilico section, is set to 0.08 Myr, while the duration of the Mortilleti Subzone is set to 0.25 Myr.

The age of the Barremian/Aptian boundary differs here by ~5 Myr from the Geologic Time Scale 2016 (Ogg et al., 2016). Recently, Olierook et al. (2019) revised the age of the base of magnetochron M0r at 123.8 to 121.8 Ma from a synthesis of available radiometric data worldwide distributed. Intercalibration between biostratigraphy and magnetostratigraphy remains uncertain around the Barremian-Aptian boundary due to the scarcity of ammonites and the lack of planktonic foraminifer or calcareous nannofossil marker (Frau et al., 2018a). Recent reattribution of ammonite specimens in Northern Italy document the presence of *Barguesiella mantei* above the top of chron M0r (Frau et al., 2018a). This species dates the lower part of the Sarasini Zone in Southern France (Frau et al., 2016), which leaves open the possibility that part of the M0r could correlate with the Giraudi Zone. Carbon-isotope stratigraphy suggest that magnetochron M0r ends within the C-isotope excursion linked to the Taxy Episode (Frau et al., 2018a). According to these data, the largest possible range of ages of magnetochron M0r is comprised between  $122.25 \pm 0.22$  Ma (age of the base of the Giraudi Zone) and  $121.38 \pm 0.21$  Ma (age of the top of the Taxy Event). This falls within the range of the ages proposed by Olierook et al. (2019). Fig. 16 and Tables 1–4 provide the proposition of the revision of the ages of the Barremian Stage and its biostratigraphic subdivisions from this work. This change proposed here and in other geochronologic studies has considerable implications, as the ages in the Cenomanian Stage are much better constrained (Meyers et al., 2012; Batenburg et al., 2016), it implies that the duration of the Aptian/Albian time should be reduced by nearly 5 Myr.

### 7.3. A control of the 2.4-Myr cycle on the episodes of environmental change

The Faraoni, Mid-Barremian and Taxy events are the three episodes of environmental change covered in this analysis (Föllmi, 2012). These episodes correspond to increasing occurrence in organic-rich layers, documented throughout the Tethyan area and possibly

extended to the Northern Atlantic (Cecca et al., 1994; Machhour et al., 1998; Mutterlose and Boeckel, 1998; Baudin, 2005; Föllmi et al., 2012; Stein et al., 2012; Yilmaz et al., 2012; Baudin and Riquier, 2014). Kaolinite contents, changes in the carbonate producers and assemblages of pelagic planktonic communities point to more humid and maybe warmer conditions during the occurrence of these environmental events (Föllmi et al., 1994; Moiroud et al., 2012; Föllmi, 2012; Aguado et al., 2014a), which led to enhanced weathering on continents, fertilization of the upper water column and biotic changes (Company et al., 2005; Aguado et al., 2014a). Organic-rich levels do not only occur during these events. Instead, organic-rich level occurrences culminate during these events, so that they are interpreted as episodes of regional expansion of the oxygen-minimum zone (Föllmi et al., 2012).

No evidence of organic-rich levels has been found in the sections studied here, probably due to their paleobathymetry, out of the oxygen minimum zone (de Gea et al., 2008; Sauvage et al., 2013). The equivalent levels of the Faraoni and Mid-Barremian events have been nonetheless identified in the Arroyo Gilico section from biostratigraphy and carbon-isotope stratigraphy (Company et al., 2005; Aguado et al., 2014a; Fig. 2). In the Barranco de Cavila section, a negative excursion in the  $\delta^{13}\text{C}_{\text{carb}}$  values occurs within the Sarasini Zone, which correlates to the Taxy Event (Föllmi et al., 2012; Stein et al., 2012; Frau et al., 2018a; Fig. 14). The Taxy Levels were initially identified as widespread organic-rich layers within the Sarasini Zone in the Southern Provence Basin (Moullade et al., 1998). Recent biostratigraphic revisions suggest these organic-rich layers appear during the Giraudi Zone (Frau et al., 2016) and envelop the negative excursion of the  $\delta^{13}\text{C}_{\text{carb}}$  values observed in the Sarasini Zone (Stein et al., 2012). We thus define the Taxy Event from the base of the Giraudi Zone (Frau et al., 2018b) to the increase in the  $\delta^{13}\text{C}_{\text{carb}}$  values in the Barremian-Aptian transition (Fig. 3). At regional scale, the Taxy Episode corresponds to a progressive increase in areas where organic-rich deposits are documented rather than a sudden event (Föllmi,

2012), which makes the base of this event uneasy to correlate from a basin to another. To make easier large-scale correlations, we also define the latest Barremian  $\delta^{13}\text{C}_{\text{carb}}$  negative excursion, which extends from the lower Sarasini Zone to the Barremian-Aptian transition (Fig. 3).

From the time scale proposed here, the onset of the Mid-Barremian Event occurred 2.02 Myr after the start of the Faraoni Event and preceded by 2.43 Myr the start of the Taxy Event and by 2.75 Myr the start of the latest Barremian C-isotope excursion. A mean duration of 2.23 Myr thus separates the onset of Faraoni, Mid-Barremian and Taxy Episodes of Environmental Changes. These durations fall into the variability of the 2.4-Myr eccentricity cycle (Laskar et al., 2011; see Supplement 2). Grand eccentricity cycles have already proven to be linked to episodes of acceleration of the continental weathering and episodes of environmental changes in the Early Cretaceous, notably during the Valanginian-Hauterivian stages (Kujau et al., 2013; Charbonnier et al., 2016; Martinez, 2018). Mercury data suggest that volcanic pulses occurred during the Dalaris Zone, i.e. ~375 kyr before the Faraoni Event, in the Upper part of the Nickles Zone, i.e. ~500 kyr before the Mid-Barremian Event, and within the Taxy Event (Charbonnier et al., 2018). Decreased trends in lead and osmium-isotope ratios are observed during the negative carbon-isotope excursion of the Taxy Event (Tejada et al., 2009; Kurda et al., 2011). The increase in volcanic activity observed during the latest Hauterivian–Barremian interval may have notably enhanced the expression of Taxy Event. Nonetheless, according to the time scale proposed here, the grand orbital cycles punctuate the pacing of the episodes of environmental change from the latest Hauterivian to the Barremian.

In the Valanginian–Hauterivian times, the peaks of humid conditions led to increase in detrital supply and, thus, increase in the sedimentation rate in the Vocontian Basin (Martinez, 2018). Here, the Faraoni, Taxy and Mid-Barremian events occur during minima or long-term

decrease of the MS values and sedimentation rates, which also show a mean period of ~2.4 Myr (Fig. 16). The changes in the sedimentation rates are coeval with the Río Argos section and are thus related processes which are at least basin-scale. The Faraoni, Mid-Barremian and Taxy events occur at time where the marl beds are thinner leading to lower sedimentation rates and increased CaCO<sub>3</sub> content of the sediment. This seems to be a paradox as more humid conditions usually lead to more detrital supply to the basin (Martinez, 2018). These three events are concomitant to 2<sup>nd</sup>-order maximum flooding events identified in Western Tethys facies (Hardenbol et al., 1998; Baudin, 2005; Fig. 16), 3<sup>rd</sup>-order sea-level highs identified in the Arabian Platform and attributed to the 2.4 Myr cycle (Matthews and Frohlich, 2002) and to regional drowning events of the carbonate platforms and extension of basin facies in the French and Swiss Alps (Bodin et al., 2006b; Frau et al., 2016, 2020). The reduced sedimentation rate observed in the three sections during the Faraoni, the Mid-Barremian and the Taxy events could be a consequence of basin starvation at a time of fastest rise in sea level. Periods of increasing sea level are notably responsible for the flooding of continental shelves where the primary productivity is the highest (Jarvis et al., 2002). Thus, the 2.4-Myr eccentricity cycle appear to have impacted both the hydrological cycle and the sea level. These periods of increased nutrient input to basins and increased sea level favored marine primary productivity and expansion of dysoxic to anoxic conditions through the Tethys and Western Europe from the latest Hauterivian to the Barremian stages.

## Conclusions

An integrated astrochronologic framework is performed from magnetic susceptibility data and CaCO<sub>3</sub> contents measured in two section of the Subbetic Domain and correlated to other reference sections. The 405-kyr eccentricity is notably identified from frequency ratio comparison and correlations to other sections. The duration of the Barremian Stage is

assessed here at  $4.58^{+0.15}_{-0.29}$  Myr. According to our time scale, the Barremian Stage started  $125.98 \pm 0.21$  Ma and ended  $121.40 \pm 0.34$  Ma. The ages of the boundaries of ammonite zones/subzones, together with those of the calcareous nannofossil subzones and events are also provided here. The Faraoni, mid-Barremian and Taxy events show a pacing of 2.2 Myr on average, which can be related to the period of the 2.4-Myr eccentricity cycle. The astronomical pacing punctuated the recurrence of episodes of environmental change through changes in continental weathering, sea level and primary productivity in basin environments. In the Subbetic Domain, it also impacted the sedimentation rate at basin scale. The episodes of environmental change occurred during minima in the sedimentation rate which correlate to higher sea level and have probably caused basin starvation.

### **Acknowledgments**

This study was funded by research project CGL2014-52546-P (Ministerio de Ciencia, Innovación y Universidades, Spain) and RNM-200 and 373 Research Groups (Junta de Andalucía, Spain). We want express our gratitude to M.J. Campos and N. Siles, for their collaboration in the determination of the carbonate content. All the authors collected the samples in the field. This study was designed by LOD, MC, RA and MM. MM measured the magnetic susceptibility, made the spectral analyses and the astrochronologic time scale. RA determined the calcareous nannofossils and provided with the calcareous nannofossil scheme and the calcium carbonate content. MC provided with the ammonite biostratigraphic scheme of the sections and the correlation with Río Argos. The data provided here have been deposited at Pangaea (<https://issues.pangaea.de/browse/PDI-22807>). We acknowledge Andy Gale, Stéphane Bodin and three anonymous reviewers for their enthusiastic and constructive comments which contributed to improve the manuscript.

### Figure and table captions

**Fig. 1.** Geological setting of the studied sections. A, Location of the Subbetic Domain and other sections mentioned in the text in the Western Tethys area (from Barrier et al., 2018). B, Picture of the Barranco Cavila section in the Sartousiana Zone with interpretations of the 100-kyr eccentricity cycles (labelled “e” in the figure). C, Simplified geological map of the Subbetic Domain with location of the Arroyo Gilico and the Barranco Cavila sections. D, Climatic model of deposit of the marl-limestone alternations in pelagic areas in the western Tethys (from Mutterlose and Ruffell, 1999). E, Hypothetical paleogeographic section of the Southern Iberian Continental Margin indicating the locations of Barranco Cavila and the Arroyo Gilico sections (modified from Aguado et al., 2018).

**Fig. 2.** Ammonite zones/subzones, calcareous nannofossil subzones and events, magnetic susceptibility (MS), CaCO<sub>3</sub> content, and carbon and oxygen isotope stratigraphy (after Aguado et al., 2014a) of the Arroyo de Gilico section. Shaded horizontal bands correspond to the positions of the Faraoni and Mid-Barremian episodes. The red lines correspond to the long-term trends of the series.

**Fig. 3.** Ammonite zones/subzones, calcareous nannofossil subzones and events, magnetic susceptibility (MS), CaCO<sub>3</sub> content, and carbon and oxygen isotope stratigraphy of the Barranco de Cavila section. Shaded horizontal bands correspond to the positions of the Taxy Event. The red lines correspond to the long-term trends of the series.

**Fig. 4.** Cross-polarized and SEM micrographs of some significant calcareous nannofossils from Barranco de Cavila and type materials. A–D (reproduced from Roth and Thierstein, 1972; Thierstein, 1973). A, C, SEM micrographs of the holotype and hypotype of *Hayesites irregularis*; B, D, cross-polarized micrographs of the same specimens. E–N, cross-polarized

light micrographs of calcareous nannofossils from the Barranco de Cavila section. E–H, specimens of *Hayesites irregularis* (subcircular). I–L, specimens of elongated *Hayesites irregularis* (morphotype E). M, *Lithraphidites magnus*. N, *Lithraphidites* sp. cf. *L. magnus*.

**Fig. 5.** Cross-plots of the magnetic susceptibility vs. CaCO<sub>3</sub> contents in the Arroyo Gilico and Barranco de Cavila sections. The solid line represents the best-fit linear regression and the dashed lines the 95% confidence intervals.

**Fig. 6.**  $2\pi$ -Multi-Taper Method (MTM) spectra, with periods labelled in meters above the spectral peaks, and COefficient COrrelation (COCO) analyses in the Arroyo Gilico section in the whole section and per interval.

**Fig. 7.** Spectrogram performed on the Arroyo Gilico section on (A) 30-m width windows and (B) 15-m width windows. The periods are labelled in meters. C, H<sub>0</sub> significance level for each sedimentation rate calculated from eCOCO analysis performed on 20-m width windows.

**Fig. 8.**  $2\pi$ -Multi-Taper Method (MTM) spectra, with periods labelled in meters above the spectral peaks, and COrrelation COefficient (COCO) analyses in the Barranco de Cavila per interval.

**Fig. 9.** Spectrogram performed on (A) 15-m width windows and (B) 7-m width windows on Interval 4 of the Barranco de Cavila section. The periods are labelled in meters. C, H<sub>0</sub> significance level for each sedimentation rate calculated from eCOCO analysis performed on 7-m width windows.

**Fig. 10.** Spectrogram performed on (A) 40-m width windows and (B) 15-m width windows on Interval 5 of the Barranco de Cavila section. The periods are labelled in meters. C, H<sub>0</sub> significance level for each sedimentation rate calculated from eCOCO analysis performed on 15-m width windows.

**Fig. 11.** Astrochronology of the interval from the Balearis to the Hugii Zone in the Río Argos and Arroyo Gilico sections. The red bandpass filters reflect the 405-kyr eccentricity cycle, the orange bands reflect the 100-kyr eccentricity cycle, the green band reflects the obliquity cycle and the blue band reflects the precession cycle. The filters of the 100-kyr and the 405-kyr eccentricity at Río Argos are from Martinez et al. (2015). The 405-kyr and 100-kyr eccentricity numbers are from Martinez et al. (2015) revised in Aguirre-Urreta et al. (2019). The parameters of the filters used in Arroyo Gilico are indicated below the figure. In each of the bandpass filters, the two frequency cuts indicated respectively correspond (from up to down) to the low and high frequency cuts.

**Fig. 12.** Astrochronology of the interval from the Hugii to the Moutonianum Zone in the Arroyo Gilico section compared to the bed counting in the Angles section in the same interval. The parameters of the filters used in Arroyo Gilico are indicated below the figure. In each of the bandpass filters, the two frequency cuts indicated respectively correspond (from up to down) to the low and high frequency cuts.

**Fig. 13.** Astrochronology of the interval around the Vandenheckii Zone in the Arroyo Gilico and Barranco de Cavila section. The parameters of the filters are indicated below the figure. In each of the bandpass filters, the two frequency cuts indicated respectively correspond (from up to down) to the low and high frequency cuts.

**Fig. 14.** Astrochronology of the interval from the Sartousiana to the Oglanlensis Zone in the Barranco de Cavila section compared to the bed counting in the Angles section from the Giraudi to the Sarasini Zone. The biostratigraphic boundaries is from Delanoy (1997). The parameters of the filters are indicated below the figure. In each of the bandpass filters, the two frequency cuts indicated respectively correspond (from up to down) to the low and high frequency cuts.

**Fig. 15.** Models of age uncertainty of (A) the Arroyo Gilico section and (B) the Barranco de Cavila section. The red dashed line represents the age model, the grey area represents 95% of the ages simulated from 1,000 of random paths, the black dashed lines represent the boundaries in depths and ages of the 405-kyr cycles.

**Fig. 16.** Revised geologic time scale of the Barremian Stage with the calibrated composite magnetic susceptibility data, the sedimentation rates of the Arroyo Gilico and Barranco de Cavila sections plotted against the 2<sup>nd</sup>-order sequence stratigraphy from Hardenbol et al. (1998). Abbreviations: T: Transgression; R: Regression. The composite magnetic susceptibility series gathers the data from Arroyo Gilico, from 127.22 to 123.42 Ma, and from Barranco de Cavila from 123.41 to 121.11 Ma. The long-term trend was obtained using a Taner lowpass filter with a frequency cut of  $8.091 \times 10^{-1}$  and a roll-off rate of  $10^{36}$ .

**Table 1.** Ages and durations of the (sub-)stages studied here. Global uncertainty corresponds to the uncertainty accounting for the age uncertainty of the base of the Krenkeli Zone, used to anchor the floating astronomical time proposed here.

**Table 2.** Ages and durations of the Tethyan ammonite (sub-)zones studied here. Notes: a: From Aguirre-Urreta et al. (2019); b: adjusted to the astrochronology from the Río Argos section from Martínez et al. (2012).

**Table 3.** Ages and durations of calcareous nannofossil events and subzones

**Table 4.** Ages and durations of the Episodes of Environmental Change of the Late Hauterivian–Barremian

## References

Aguado, R., Company, M., Castro, J.M., de Gea, G.A., Molina, J.M., Nieto, L.M., Ruiz-Ortiz, P.A., 2018. A new record of the Weissert episode from the Valanginian succession of Cehegín (Subbetic, SE Spain): Bio- and carbon isotope stratigraphy. *Cretaceous Res.* 92, 122–137. <https://doi.org/10.1016/j.cretres.2018.07.010>.

Aguado, R., Company, M., Martínez, M., Martínez-López, F.J., O'Dogherty, L., Sánchez-Bellón, A., Sandoval, J., 2017. Bioestratigrafía de alta precisión del Barremiense mediterráneo mediante nanofósiles calcáreos, in: O'Dogherty, L. (Ed.), XXXIII Jornadas de Paleontología. Libro de Resúmenes. Sociedad Española de Paleontología de España, Cadiz, pp. 11–15. <http://sepaleontologia.es/wp-content/uploads/2017/10/33SEP.pdf>.

Aguado, R., Company, M., O'Dogherty, L., Palomo, I., Sandoval, J., Tavera, J.M., 2008. Integrated stratigraphy of the uppermost Hauterivian-lower Barremian pelagic sequence of Arroyo Gilico (Betic Cordillera, SE Spain), in: Lukedener, A. (Ed.), First International Meeting on Correlations of Cretaceous Micro- and Macrofossils. Natural History Museum Vienna, Vienna, pp. 36–37. [https://www.nhm-wien.ac.at/jart/prj3/nhm/data/uploads/mitarbeiter\\_dokumente/lukeneder/2008/BR0074\\_001\\_A.pdf](https://www.nhm-wien.ac.at/jart/prj3/nhm/data/uploads/mitarbeiter_dokumente/lukeneder/2008/BR0074_001_A.pdf).

Aguado, R., Company, M., O'Dogherty, L., Sandoval, J., Tavera, J.M., 2014a. Late Hauterivian-early Barremian calcareous nannofossil biostratigraphy, palaeoceanography, and stable isotope record in the Subbetic domain (southern Spain). *Cretaceous Res.* 49, 105–124. <https://doi.org/10.1016/j.cretres.2014.02.006>.

Aguado, R., Company, M., Sandoval, J., Tavera, J.M., 1997. Biostratigraphic events at the Barremian/Aptian boundary in the Betic Cordillera, southern Spain. *Cretaceous Res.* 18, 309–329. <https://doi.org/10.1006/cres.1997.0069>.

Aguado, R., Company, M., Tavera, J.M., 2000. The Berriasian/Valanginian boundary in the Mediterranean region. New data from the Caravaca and Cehegín sections (SE Spain). *Cretaceous Res.* 21, 1–21. <https://doi.org/10.1006/cres.2000.0198>.

Aguado, R., de Gea, G.A., Castro, J.M., O'Dogherty, L., Quijano, M.L., Naafs, B.D.A., Pancost, R.D., 2014b. Late Barremian–early Aptian dark facies of the Subbetic (Betic Cordillera, southern Spain): Calcareous nannofossil quantitative analyses, chemostratigraphy and palaeoceanographic reconstructions. *Palaeogeogr., Palaeoclimatol., Palaeoecol.* 395, 198–221. <https://doi.org/10.1016/j.palaeo.2013.12.031>.

Aguirre-Urreta, B., Lescano, M., Schmitz, M. D., Tunik, M., Concheyro, A., Rawson, P. F., Ramos, V. A., 2015. Filling the gap: new precise Early Cretaceous radioisotopic ages from the Andes. *Geol. Mag.* 152, 557–564. <https://doi.org/10.1017/S001675681400082X>.

Aguirre-Urreta, B., Schmitz, M., Lescano, M., Tunik, M., Rawson, P.F., Concheyro, A., Buhler, M., Ramos, V.A., 2017. A high precision U–Pb radioisotopic age for the Agrio Formation, Neuquén Basin, Argentina: Implications for the chronology of the Hauterivian Stage. *Cretaceous Res.* 75, 193–205. <https://doi.org/10.1016/j.cretres.2017.03.027>.

Aguirre-Urreta, B., Martínez, M., Schmitz, M., Lescano, M., Omarini, J., Tunik, M., Kuhnert, H., Concheyro, A., Rawson, P.F., Ramos, V.A., Reboulet, S., Noclin, N., Frederichs, T., Nickl, A.-L., Pälike, H., 2019. Interhemispheric radio-astrochronological calibration of the time scales from the Andean and the Tethyan areas in the Valanginian-Hauterivian (Early Cretaceous). *Gondwana Res.* 70, 104–132. <https://doi.org/10.1016/j.gr.2019.01.006>.

Baccelle, L., Bosellini, A., 1965. Diagrammi per la stima visiva della composizione percentuale nelle rocce sedimentarie. *Annali Università di Ferrara. Sezione IX Scienze Geologiche e Paleontologiche* 1, 59–62.

Barrier, E., Vrielynck, B., Brouillet, J.-F., Brunet, M.-F., 2018. Paleotectonic Reconstruction of the of the Central Tethyan Realm, CCGM-CGMW, Paris.

Batenburg, S.J., De Vleeschouwer, D., Sprovieri, M., Hilgen, F.J., Gale, A.S., Singer, B.S., Koeberl, C., Coccioni, R., Claeys, P., Montanari, A., 2016. Orbital control on the timing of oceanic anoxia in the Late Cretaceous. *Clim. Past* 12, 1995–2009. <https://doi.org/10.5194/cp-12-1995-2016>.

Baudin, F., 2005. A Late Hauterivian short-lived anoxic event in the Mediterranean Tethys: the 'Faraoni Event'. *C. R. Geosci.* 337, 1532–1540. <https://doi.org/10.1016/j.crte.2005.08.012>.

Baudin, F., Riquier, L., 2014. The Late Hauterivian Faraoni 'Oceanic Anoxic Event': an update. *Bull. Soc. Geol. Fr.* 185, 359–377. <https://doi.org/10.2113/gssgfbull.185.6.359>.

Baudin, F., Faraoni, P., Marini, A., Pallini, G., 1998. Organic matter characterization of the 'Faraoni Level' from Northern Italy (Lessini Mountains and Trento Plateau): comparison with that from Umbria–Marche Apennines. *Palaeopelagos* 7, 41–51.

Bodin, S., Godet, A., Föllmi, K.B., Vermeulen, J., Arnaud, H., Strasser, A., Fiet, N., Adatte, T., 2006a. The late Hauterivian Faraoni oceanic anoxic event in the western Tethys: Evidence from phosphorus burial rates. *Palaeogeogr., Palaeoclimatol., Palaeoecol.* 235, 245–264. <https://doi.org/10.1016/j.palaeo.2005.09.030>.

Bodin, S., Godet, A., Vermeulen, J., Linder, P., Föllmi, K.B., 2006b. Biostratigraphy, sedimentology and sequence stratigraphy of the latest Hauterivian – Early Barremian drowning episode of the Northern Tethyan margin (Altmann Member, Helvetic nappes, Switzerland). *Eclogae Geol. Helv.* 99, 157–174. <https://doi.org/10.1007/s00015-006-1188-7>.

Bodin, S., Meissner, P., Janssen, N.M.M., Steuber, T., Mutterlose, J., 2015. Large igneous provinces and organic carbon burial: Controls on global temperature and continental

weathering during the Early Cretaceous. *Glob. Planet. Change* 133, 238–253. <https://doi.org/10.1016/j.gloplacha.2015.09.001>.

Bown, P.R., 2005. Early to mid-Cretaceous calcareous nannoplankton from the Northwest Pacific Ocean, Leg 198, Shatsky Rise. *Proc. ODP Sci. Results* 198, 1–82. <https://doi.org/10.2973/odp.proc.sr.198.103.2005>.

Bown, P.R., Young, J.R., 1998. Techniques, in: Bown, P.R. (Ed.), *Calcareous Nannofossil Biostratigraphy*, 1 ed. Chapman & Hall, London, pp. 16–28.

Bown, P.R., Rutledge, D.C., Crux, J.A., Gallagher, L.T., 1998. Lower Cretaceous, in: Bown, P.R. (Ed.), *Calcareous Nannofossil Biostratigraphy*, 1 ed. Chapman and Hall, London, pp. 86–131.

Bralower, T.J., Leckie, R.M., Sliter, W.V., Tierstein, H.R., 1995. An integrated Cretaceous microfossil biostratigraphy, in: Berggren, W.A., Kent, D.V., Aubry, M.-P., Hardenbol, J. (Eds.), *Geochronology, Time Scales and Global Stratigraphic Correlation*. SEPM Spec. Publ. 54, Tulsa, OK, pp. 65–79. <https://doi.org/10.2110/pec.95.04.0065>.

Cecca, F., Marini, A., Pallini, G., Baudin, F., Begouen, V., 1994. A guide-level of the uppermost Hauterivian (Lower Cretaceous) in the pelagic succession of Umbria-Marche Apennines (Central Italy): the Faraoni Level. *Riv. Ital. Paleontol. Stratigr.* 99, 551–568.

Charbonnier, G., Duchamp-Alphonse, S., Adatte, T., Föllmi, K.B., Spangenberg, J.E., Gardin, S., Galbrun, B., Colin, C., 2016. Eccentricity paced monsoon-like system along the northwestern Tethyan margin during the Valanginian (Early Cretaceous): New insights from detrital and nutrient fluxes into the Vocontian Basin (SE France). *Palaeogeogr., Palaeoclimatol., Palaeoecol.* 443, 145–155. <https://doi.org/10.1016/j.palaeo.2015.11.027>.

Charbonnier, G., Godet, A., Bodin, S., Adatte, T., Follmi, K.B., 2018. Mercury anomalies, volcanic pulses, and drowning episodes along the northern Tethyan margin during the latest Hauterivian-earliest Aptian. *Palaeogeogr., Palaeoclimatol., Palaeoecol.* 505, 337–350. <https://doi.org/10.1016/j.palaeo.2018.06.013>.

Cleveland, W.S., 1979. Robust locally weighted regression and smoothing scatterplots. *J. Am. Stat. Assoc.* 74, 829–836. <https://doi.org/10.2307/2286407>.

Cohen, K.M., Finney, S.C., Gibbard, P.L., Fan, J.-X., 2013. The ICS International Chronostratigraphic Chart. *Episodes* 36, 199–204, last update: March 2020. <https://doi.org/10.18814/epiiugs/2013/v36i3/002>; URL to the update ICS Geologic Time Scale: <https://stratigraphy.org/chart>. Company, M., Aguado, R., Jiménez de Cisneros, C., Sandoval, J., Tavera, J.M., Vera, J.A., 2003a. Biotic changes at the Hauterivian/Barremian boundary in the Mediterranean Tethys, in: Lamolda, M.A. (Ed.), *Bioevents: their Stratigraphical Records, Patterns and Causes*. Field-Trip Guide 1. Ayuntamiento de Caravaca de la Cruz, Caravaca de la Cruz (Murcia), pp. 15–28.

Company, M., Sandoval, J., Tavera, J.M., 2003b. Ammonite biostratigraphy of the uppermost Hauterivian in the Betic Cordillera (SE Spain). *Cretaceous Res.* 36, 685–694. <https://doi.org/10.1016/j.cretres.2002.12.001>.

Company, M., Sandoval, J., Tavera, J.M., 2004. El Barremiense de Fontcalent y L'Alcoraia (Alicante). *Geo-Temas* 7, 217–221.

Company, M., Aguado, R., Sandoval, J., Tavera, J.M., de Cisneros, C.J., Vera, J.A., 2005. Biotic changes linked to a minor anoxic event (Faraoni Level, latest Hauterivian, early Cretaceous). *Palaeogeogr., Palaeoclimatol., Palaeoecol.* 224, 186–199. <https://doi.org/10.1016/j.palaeo.2005.03.034>.

Covington, J.M., Wise, S.W., Jr., 1987. Calcareous nannofossil biostratigraphy of a Lower Cretaceous deep-sea fan complex: Deep Sea Drilling Project Leg 93, Site 603, lower continental rise off Cape Hatteras. *Init. Repts. DSDP 93*, 617–660. <https://doi.org/10.2973/dsdp.proc.93.116.1987>.

de Gea, G.A., 2004. Bioestratigrafía y eventos del Cretácico Inferior en las Zonas Externas de la Cordillera Bética. PhD Thesis. Servicio de Publicaciones de la Universidad de Jaén, Jaén.

de Gea, G.A., Aguado, R., Castro, J.M., Molina, J.M., O'Dogherty, L., Ruiz-Ortiz, P.A., 2008. Lower Aptian Subbetic organic-rich facies, radiolarites, and associated deposits: the local expression of Oceanic Anoxic Event 1a (Carbonero Formation, southern Spain). *Cretaceous Res.* 29, 861–870. <https://doi.org/10.1016/j.cretres.2008.05.011>.

Delanoy, G., 1997. Biostratigraphie des faunes d'ammonites à la limite Barrémien–Aptien dans la région d'Angles–Barrême–Castellane. Étude particulière de la famille des Heteroceratidae Spath, 1922 (Ancyloceratina, Ammonoidea). *Annales du Muséum d'Histoire Naturelle de Nice* 12, 1–270.

Fiet, N., Gorin, G., 2000. Lithological expression of Milankovitch cyclicity in carbonate-dominated, pelagic, Barrémian deposits in central Italy. *Cretaceous Res.* 21, 457–467. <https://doi.org/10.1006/cres.2000.0220>.

Föllmi, K.B., 2012. Early Cretaceous life, climate and anoxia. *Cretaceous Res.* 35, 230–257. <https://doi.org/10.1016/j.cretres.2011.12.005>.

Föllmi, K.B., Bole, M., Jammet, N., Froidevaux, P., Godet, A., Bodin, S., Adatte, T., Matera, V., Fleitmann, D., Spangenberg, J.E., 2012. *Clim. Past* 8, 171–189. <https://doi.org/10.5194/cp-8-171-2012>.

- Föllmi, K.B., Weissert, H., Bisping, M., Funk, H., 1994. Phosphogenesis, carbon-isotope stratigraphy, and carbonate-platform evolution along the lower Cretaceous northern Tethyan margin. *Geol. Soc. Am. Bull.* 106, 729–746. [https://doi.org/10.1130/0016-7606\(1994\)106<0729:PCISAC>2.3.CO;2](https://doi.org/10.1130/0016-7606(1994)106<0729:PCISAC>2.3.CO;2).
- Frau, C., Bulot, L.G., Delanoy, G., Moreno-Bedmar, J.A., Masse, J.-P., Tendil, A.J.-B., Lanteaume, C., 2018a. The Aptian GSSP candidate at Gorgo a Cerbara (Central Italy): an alternative interpretation of the bio-, litho- and chemostratigraphic markers. *Newsl. Stratigr.* 51, 311 – 326. <https://doi.org/10.1127/nos/2017/0422>.
- Frau, C., Delanoy, G., Masse, J.-P., Lanteaume, C., Tendil, A.J.B., 2016. New Heteroceratidae (Ammonoidea) from the late Barremian deepening succession of Marseille (Bouches-du-Rhône, France). *Acta Geol. Pol.* 66, 205–225. <https://doi.org/10.1515/agp-2016-0009>.
- Frau, C., Tendil, A. J.-B., Lanteaume, C., Masse, J.-P., Pictet, A., Bulot, L.G., Lubert, T.L., Redfern, J., Borgomano, J.R., Leonice, P., Fournier, F., Massonnat, G., 2018b. Late Barremian–early Aptian ammonite bioevents from the Urgonian-type series of Provence, southeast France: Regional stratigraphic correlations and implications for dating the peri-Vocontian carbonate platforms. *Cretaceous Res.* 90, 222–253. <https://doi.org/10.1016/j.cretres.2018.04.008>.
- Frau, C., Tendil, A. J.-B., Pohl, A., Lanteaume, C., 2020. Revising the timing and causes of the Urgonian rudistid-platform demise in the Mediterranean Tethys. *Glob. Planet. Change* 187, 103124. <https://doi.org/10.1016/j.gloplacha.2020.103124>.
- Gradstein, F.M, Ogg, J.G., Schmitz, M.D., Ogg, G.M., 2012. *The Geologic Time Scale 2012*. Elsevier B.V., Amsterdam.

Hardenbol, J., Thierry, J., Farley, M.B., Jacquin, T., de Graciansky, P.-C., Vail, P.R., 1998. Mesozoic and Cenozoic sequence stratigraphy of European basins. *SEPM Spec. Publ.* 60, Tulsa, OK.

Haslett, J., Parnell, A., 2008. A simple monotone process with application to radiocarbon-dated depth chronologies. *J. R. Stat. Soc. Ser. C-Apl. Stat.* 57, 399–418. <https://doi.org/10.1111/j.1467-9876.2008.00623.x>.

Herbert, T.D., de Boer, P.L., Smith, D.G., 1994. Reading orbital signals distorted by sedimentation: models and examples, in: P.L. de Boer and D.G. Smith, *Orbital forcing and cyclic sequences*, *IAS Spec. Publ.* 19, pp. 483–507. <https://doi.org/10.1002/9781444304039.ch29>.

Hoedemaeker, P.J., Hengreen, G.F.W., 2003. Correlation of Tethyan and Boreal Berriasian - Barremian strata with emphasis on strata in the subsurface of the Netherlands. *Cretaceous Res.* 24, 253–275. [https://doi.org/10.1016/S0195-6671\(03\)00044-2](https://doi.org/10.1016/S0195-6671(03)00044-2).

Hoedemaeker, P.J., Leereveld, H., 1995. Biostratigraphy and sequence stratigraphy of the Berriasian-lowest Aptian (lower Cretaceous) of the Rio-Argos succession, Caravaca, SE Spain. *Cretaceous Res.* 16, 195–230. <https://doi.org/10.1006/cres.1995.1016>.

Hunt, C.P., Moskowitz, B.M. and Banerjee, S.K., 1995. Magnetic Properties of Rocks and Minerals, in: Ahrens, T.J. (Ed.), *Rock Physics and Phase Relations: A Handbook of Physical Constants*. AGU Reference Shelf, 3. American Geophysical Union, Washington DC, USA, pp. 189–204.

Jarvis, I., Mabrouk, A., Moody, R.T.J., de Cabrera, S., 2002. Late Cretaceous (Campanian) carbon isotope events, sea-level change and correlation of the Tethyan and Boreal realms. *Palaeogeography, Palaeoclimatology, Palaeoecology* 188, 215–248. [https://doi.org/10.1016/S0031-0182\(02\)00578-3](https://doi.org/10.1016/S0031-0182(02)00578-3).

- Kujau, A., Heimhofer, U., Hochuli, P.A., Pauly, S., Morales, C., Adatte, T., Föllmi, K., Ploch, I., Mutterlose, J., 2013. Reconstructing Valanginian (Early Cretaceous) mid-latitude vegetation and climate dynamics based on spore-pollen assemblages. *Rev. Palaeobot. Palynology* 197, 50–69. <https://doi.org/10.1016/j.revpalbo.2013.05.003>.
- Kuroda, J., Tanimizu, M., Hori, R.S., Suzuki, K., Ogawa, N.O., Tejada, M.L.G., Coffin, M.F., Coccioni, R., Erba, E., Ohkouchi, N., 2011. Lead isotopic record of Barremian–Aptian marine sediments: Implications for large igneous provinces and the Aptian climatic crisis. *Earth Planet. Sci. Lett.* 307, 126–134. <https://doi.org/10.1016/j.epsl.2011.04.021>.
- Laskar, J., Fienga, A., Gastineau, M., Manche, H., 2011a. L<sub>2010</sub>: a new orbital solution for the long-term motion of the Earth. *Astron. Astrophys.* 532, A89. <https://doi.org/10.1051/0004-6361/201116836>.
- Laskar, J., Robutel, P., Joutel, F., Gastineau, M., Correia, A.C.M., Levrard, B., 2004. A long-term numerical solution for the insolation quantities of the Earth. *Astron. Astrophys.* 428, 261–285. <https://doi.org/10.1051/0004-6361:20041335>.
- Lena, L., López-Martínez, R., Escano, M., Aguirre-Urreta, B., Concheyro, A., Vennari, V., Naipauer, M., Samankasson, E., Pimentel, M., Ramos, V.A., Schaltegger, U., 2019. High-precision U–Pb ages in the early Tithonian to early Berriasian and implications for the numerical age of the Jurassic–Cretaceous boundary. *Solid Earth* 10, 1–14. <https://doi.org/10.5194/se-10-1-2019>.
- Li, M.S., Kump, L.R., Hinnov, L.A., Mann, M.E., 2018. Tracking variable sedimentation rates and astronomical forcing in Phanerozoic paleoclimate proxy series with evolutionary correlation coefficients and hypothesis testing. *Earth Planet. Sci. Lett.* 501, 165–179. <https://doi.org/10.1016/j.epsl.2018.08.041>.

- Machhour, L., Masse, J.-P., Oudin, J.-L., Lambert, B., Lapointe, P., 1998. Petroleum potential of dysaerobic carbonate source rocks in an intra-shelf basin: the Lower Cretaceous of Provence, France. *Petrol. Geosci.* 4, 139–146. <https://doi.org/10.1144/petgeo.4.2.139>.
- Mann, M.E., Lees, J.M., 1996. Robust estimation of background noise and signal detection in climatic time series. *Clim. Change* 33, 409–445. <https://doi.org/10.1007/BF00142586>.
- Martinez, M., 2018. Chapter Four - Mechanisms of Preservation of the Eccentricity and Longer-term Milankovitch Cycles in Detrital Supply and Carbonate Production in Hemipelagic Marl-Limestone Alternations, in: M. Monenari (Ed.), *Stratigraphy and Timescales*, volume 3 *Cyclostratigraphy and Astrochronology*, Elsevier B.V., Amsterdam, pp. 189–218. <https://doi.org/10.1016/bs.sats.2018.08.002>.
- Martinez, M., Deconinck, J.-F., Pellenard, P., Reboulet, S., Riquier, L., 2013. Astrochronology of the Valanginian Stage from reference sections (Vocontian Basin, France) and palaeoenvironmental implications for the Weissert Event. *Palaeogeogr., Palaeoclimatol., Palaeoecol.* 376, 91–102. <https://doi.org/10.1016/j.palaeo.2013.02.021>.
- Martinez, M., Deconinck, J.-F., Pellenard, P., Riquier, L., Company, M., Reboulet, S., Moiroud, M., 2015. Astrochronology of the Valanginian-Hauterivian stages (Early Cretaceous): Chronological relationships between the Parana-Etendeka large igneous province and the Weissert and the Faraoni events. *Glob. Planet. Change* 131, 158–173. <https://doi.org/10.1016/j.gloplacha.2015.06.001>.
- Martinez, M., Kotov, S., De Vleeschouwer, D., Pas, D., Pälike, H., 2016. Testing the impact of stratigraphic uncertainty on spectral analyses of sedimentary series. *Clim. Past* 12, 1765–1783. <https://doi.org/10.5194/cp-12-1765-2016>.
- Martinez, M., Pellenard, P., Deconinck, J.-F., Monna, F., Riquier, L., Boulila, S., Moiroud, M., Company, M., 2012. An orbital floating time scale of the Hauterivian/Barremian GSSP

from a magnetic susceptibility signal (Río Argos, Spain). *Cretaceous Res.* 36, 106–115.  
<https://doi.org/10.1016/j.cretres.2012.02.015>.

Matthews, R.K., Frohlich, C., 2002. Maximum flooding surfaces and sequence boundaries: comparisons between observations and orbital forcing in the Cretaceous and Jurassic (65-190 Ma). *GeoArabia* 7, 503–538.

Meyers, S.R., Siewert, S.E., Singer, B.S., Sageman, B.B., Condon, D.J., Obradovich, J.D., Jicha, B.R., Sawyer, D.A., 2012. Intercalibration of radioisotopic and astrochronologic time scales for the Cenomanian-Turonian boundary interval, Western Interior Basin, USA. *Geology* 40, 7–10. <https://doi.org/10.1130/G32261.1>.

Moiroud, M., Martinez, M., Deconinck, J.-F., Monna F., Pellenard, P., Riquier, L., Company, M., 2012. High-resolution clay mineralogy as a proxy for orbital tuning: Example of the Hauterivian-Barremian transition in the Betic Cordillera (SE Spain). *Sediment. Geol.* 282, 336–346. <https://doi.org/10.1016/j.sedgeo.2012.10.004>.

Moullade, M., Masse, J.-P., Tronchetti, G., Kuhnt, W., Ropolo, P., Bergen, J.-A., Masure E., Renard, M., 1998. Le stratotype historique de l'Aptien inférieur (région de Cassis-La Bédoule) : synthèse stratigraphique. *Geol. Mediterr.* 25, 289–298.

Mutterlose, J., Böckel, B., 1998. The Barremian - Aptian interval in NW Germany: a review. *Cretaceous Res.* 19, 539–568. <https://doi.org/10.1006/cres.1998.0119>.

Mutterlose, J., Ruffell, A., 1999. Milankovitch-scale palaeoclimate changes in pale-dark bedding rhythms from the Early Cretaceous (Hauterivian and Barremian) of eastern England and northern Germany. *Palaeogeogr., Palaeoclimatol., Palaeoecol.* 154, 133–160.  
[https://doi.org/10.1016/S0031-0182\(99\)00107-8](https://doi.org/10.1016/S0031-0182(99)00107-8).

Ogg, J.G., Ogg, G.M., Gradstein, F.M., 2016. A Concise Geologic Time Scale 2016. Elsevier B.V., Amsterdam.

Olierook, H.K.H, Jourdan, F., Merle, R.E., 2019. Age of the Barremian–Aptian boundary and onset of the Cretaceous Normal Superchron. *Earth-Sci. Rev.*, 102906. <https://doi.org/10.1016/j.earscirev.2019.102906>.

Perch-Nielsen, K., 1985. Mesozoic calcareous nannofossils, in: Bolli, H.M., Saunders, J.B., Perch-Nielsen, K. (Eds.), *Plankton Stratigraphy*. Cambridge University Press, Cambridge, pp. 329–426.

Premoli Silva, I., Soldan, D.M., Petrizzo, M.R., 2018. Upper Hauterivian–upper Barremian planktonic foraminiferal assemblages from the Arroyo Gilico section (Southern Spain). *J. Foraminifer. Res.* 48, 314–355. <https://doi.org/10.2113/gsjfr.48.4.314>.

Reboulet, S., Szives, O., Aguirre-Urreta, E., Barragan, R., Company, M., Frau, C., Kakabadze, M.V., Klein, J., Moreno-Bedmar, J.A., Lukeneder, A., Pictet, A., Ploch, I., Raisossadat, S.N., Vasicek, Z., Baraboshkin, E.J., Mita, V.V., 2018. Report on the 6th International Meeting of the IUGS Lower Cretaceous Ammonite Working Group, the Kilian Group (Vienna, Austria, 20th August 2017). *Cretaceous Res.* 91, 100–110. <https://doi.org/10.1016/j.cretres.2018.05.008>.

Roth, P.H., Thierstein, H.R., 1972. Calcareous nannoplankton: Leg 14 of the Deep-Sea Drilling Project. *Init. Repts. DSDP* 14, 421–485. <https://doi.org/10.2973/dsdp.proc.14.114.1972>.

Sauvage, L., Riquier, L., Thomazo, C., Baudin, F., Martinez, M., 2013. The late Hauterivian Faraoni "Oceanic Anoxic Event" At Río Argos (southern Spain): An assessment on the level of oxygen depletion. *Chemical Geology* 340, 77–90. <https://doi.org/10.1016/j.chemgeo.2012.12.004>.

- Sprenger, A., Ten Kate, W.G., 1993. Orbital forcing of calcilutite-marl cycles in Southeast Spain and an estimate for the duration of the Berriasian Stage. *Geol. Soc. Am. Bull.* 105, 807–818. [https://doi.org/10.1130/0016-7606\(1993\)105<0807:OFOCMC>2.3.CO;2](https://doi.org/10.1130/0016-7606(1993)105<0807:OFOCMC>2.3.CO;2).
- Sprovieri, M., Coccioni, R., Lirer, F., Pelosi, N., Lozar, F., 2006. Orbital tuning of a lower Cretaceous composite record (Maiolica Formation, central Italy). *Paleoceanography* 21, PA4212. <https://doi.org/10.1029/2005PA001224>.
- Stein, M., Westermann, S., Adatte, T., Matera, V., Fleitmann, D., Spangenberg, J.E., Föllmi, K.B., 2012. Late Barremian-Early Aptian palaeoenvironmental change: The Cassis-La Bedoule section, southeast France. *Cretaceous Res.* 37, 209–222. <https://doi.org/10.1016/j.cretres.2012.03.021>.
- Taner, M.T., 2003. *Attributes Revisited*, Technical Publication. Rock Solid Images, Inc., Houston, TX (URL: [rocksolidimages.com/pci/attrib\\_revisited.htm](http://rocksolidimages.com/pci/attrib_revisited.htm)).
- Tejada, M.L.G., Suzuki, K., Kuroda, I., Coccioni, R., Mahoney, J.J., Ohkouchi, N., Sakamoto, T., Tatsumi, Y., 2009. Ontong Java Plateau eruption as a trigger for the Early Aptian oceanic anoxic event. *Geology* 37, 855–858. <https://doi.org/10.1130/G25763A.1>.
- Thierstein, H.R., 1973. Lower Cretaceous calcareous nannoplankton biostratigraphy. *Abh. Geol. B.-A.* 29, 1–52.
- Thibault, N., Jarvis, I., Voigt, S., Gale, A.S., Attree, K., Jenkyns, H.C., 2016. Astronomical calibration and global correlation of the Santonian (Cretaceous) based on the marine carbon isotope record. *Paleoceanography* 31, 847–865. <https://doi.org/10.1002/2016PA002941>.
- Thomson, D.J., 1982. Spectrum estimation and harmonic analysis. *Proc. IEEE* 70, 1055–1096. <https://doi.org/10.1109/PROC.1982.12433>.

Thomson, D.J., 1990. Quadratic-Inverse Spectrum Estimates: Applications to Palaeoclimatology. *Philos. Trans. R. Soc. A-Math. Phys. Eng. Sci.* 332, 539–597. <https://doi.org/10.1098/rsta.1990.0130>.

Van Veen, G.W., 1969. Geological investigations in the region west of Caravaca, south-eastern Spain. PhD. Thesis, Univ. Amsterdam, 143 pp.

Vaughan, S., Bailey, R.J., Smith, D.G., 2011. Detecting cycles in stratigraphic data: Spectral analysis in the presence of red noise. *Paleoceanography* 26, PA4211. <https://doi.org/10.1029/2011PA002195>.

Vennari, V.V., Lescano, M., Naipauer, M., Aguirre-Urreta, B., Concheyro, A., Schaltegger, U., Armstrong, R., Pimentel, M., Ramos, V.A., 2014. New constraints on the Jurassic-Cretaceous boundary in the High Andes using high-precision U-Pb data. *Gondwana Res.* 26, 374–385. <https://doi.org/10.1016/j.gr.2013.07.005>.

Vera, J.A., 2001. Evolution of the South Iberian Continental Margin. In: P.A. Ziegler, W. Cavazza, A.H.F. Robertson and C. Crasquin-Soleau (Eds.), *Peri-Tethys Memoir 6: Peri-Tethyan Rift/Wrench Basins and Passive Margins*. Mémoires du Museum National d'Histoire Naturelle, pp. 109–143.

Vera, J.A., Arias, C., Carcía-Hernández, M., López-Garrido, A.C., Martín-Algarra, A., Martín-Chivelet, J., Molina, J.M., Rivas, P., Ruiz-Ortiz, P.A., Sanz de Galdeano, C., Vilas, L., 2004. Las Zonas Externas Béticas y el Paleomargen Sudibérico, in: Vera, J.A. (Ed.), *Geología de España*. Sociedad Geológica de España e Instituto Geológico y Minero de España, Madrid, pp. 354–361.

Yilmaz, I.O., Altiner, D., Tekin, U.K., Ocakoglu, F., 2012. The first record of the "Mid-Barremian" Oceanic Anoxic Event and the Late Hauterivian platform drowning of the Bilecik

platform, Sakarya Zone, western Turkey. Cretaceous Res. 38, 16–39.

<https://doi.org/10.1016/j.cretres.2012.04.010>.

Journal Pre-proof

Conflict of interest:

The authors declare no conflict of interest

Journal Pre-proof

Highlights:

- Duration of the Barremian Stage proposed at  $4.58^{+0.15}_{-0.29}$  Myr from astrochronology
- Ages of the Barremian Stage: ~3.5 Myr younger than in the ICS' Geologic Time Scale 2020
- Episodes of Environmental Changes paced by the 2.4-Myr eccentricity cycle

Journal Pre-proof

Base Substage	Level at Arroyo Gilico (m)	Level at Barranco Cavila (m)	Numerical age (Ma)	Uncertainty age model (Myr)	Global uncertainty (Myr)	Duration (Myr)
<b>Barremian</b>	<b>25.4</b>		<b>125.98</b>	<b>0.09</b>	<b>0.21</b>	<b>4.58</b>
<i>Early Barremian</i>	25.4		125.98	0.09	0.21	1.71
<i>Late Barremian</i>	62.5		124.27	0.14	0.24	2.87
<i>Early Aptian</i>		61.9	121.40	0.12	0.34	

**Table 1.** Ages and durations of the (sub-)stages studied here. Global uncertainty corresponds to the uncertainty accounting for the age uncertainty of the base of the Krenkeli Zone, used to anchor the floating astronomical time proposed here.

Journal Pre-proof

Base ammonite (Sub-)Zone	Level at Arroyo Gilico (m)	Level at Barranco de Cavila (m)	Numerical age (Ma)	Uncertainty age model (Myr)	Global uncertainty (Myr)	Duration (Myr)
<b>Balearis Zone (p.p.)</b>	<b>N.A.</b>		<b>127.50<sup>a</sup></b>		<b>0.19<sup>a</sup></b>	<b>N.A.</b>
<i>Krenkeli Subzone</i>	0.0		127.22 <sup>a</sup>	0.16	0.19	0.28
<i>Angulicostata Subzone</i>	8.3		126.94	0.10	0.21	0.19
<b>Ohmi Zone</b>	<b>12.6</b>		<b>126.75</b>	<b>0.09</b>	<b>0.21</b>	<b>0.77</b>
<i>Ohmi Subzone</i>	12.6		126.75	0.09	0.21	0.08 <sup>b</sup>
<i>Mortilleti Subzone</i>	13.6		126.67 <sup>b</sup>	0.12	0.22	0.25 <sup>b</sup>
<i>Picteti Subzone</i>	18.5		126.42 <sup>b</sup>	0.11	0.22	0.44
<b>Hugii Zone</b>	<b>25.4</b>		<b>125.98</b>	<b>0.09</b>	<b>0.21</b>	<b>0.57</b>
<i>Hugii Subzone</i>	25.4		125.98	0.09	0.21	0.26
<i>Colombiana Subzone</i>	30.2		125.72	0.12	0.22	0.31
<b>Nicklesi Zone</b>	<b>36.6</b>		<b>125.41</b>	<b>0.13</b>	<b>0.23</b>	<b>0.23</b>
<b>Pulchella Zone</b>	<b>42.2</b>		<b>125.18</b>	<b>0.12</b>	<b>0.22</b>	<b>0.21</b>
<b>Compressissima Zone</b>	<b>47.6</b>		<b>124.97</b>	<b>0.12</b>	<b>0.22</b>	<b>0.31</b>
<i>Fallax Subzone</i>	47.6		124.97	0.12	0.22	0.15
<i>Caillaudianus Subzone</i>	51.6		124.82	0.04	0.19	0.16
<b>Moutonianum Zone</b>	<b>54.9</b>		<b>124.65</b>	<b>0.11</b>	<b>0.22</b>	<b>0.39</b>
<b>Vandenheckii Zone</b>	<b>62.5</b>		<b>124.27</b>	<b>0.14</b>	<b>0.24</b>	<b>1.05</b>
<i>Vandenheckii Subzone</i>	62.5		124.27	0.14	0.24	0.54
<i>Alpinum Subzone</i>	69.5		123.75	0.13	0.23	0.51
<b>Sartousiana Zone</b>		<b>16.0</b>	<b>123.22</b>	<b>0.09</b>	<b>0.21</b>	<b>0.97</b>
<i>Sartousiana Subzone</i>		16.0	123.22	0.09	0.21	0.39
<i>Provincialis Subzone</i>		26.9	122.83	0.07	0.20	0.26
<i>Feraudianus Subzone</i>		35.1	122.57	0.11	0.21	0.32
<b>Giraudi Zone</b>		<b>44.2</b>	<b>122.25</b>	<b>0.12</b>	<b>0.22</b>	<b>0.15</b>
<b>Sarasini Zone</b>		<b>47.4</b>	<b>122.10</b>	<b>0.13</b>	<b>0.23</b>	<b>0.70</b>
<b>Oglanlensis Zone</b>		<b>60.9</b>	<b>121.40</b>	<b>0.12</b>	<b>0.34</b>	<b>0.19</b>
<b>Forbesi Zone</b>		<b>66.2</b>	<b>121.21</b>	<b>0.08</b>	<b>0.21</b>	<b>N.A.</b>

**Table 2.** Ages and durations of the Tethyan ammonite (sub-)zones studied here. Notes: a: From Aguirre-Urreta et al. (2019); b: adjusted to the astrochronology from the Río Argos section from Martínez et al. (2012).

Calcareous nannofossil event	Base calc. nanno. Subzone	Level at Arroyo Gilico (m)	Level at Barranco Cavila (m)	Numerical age (Ma)	Uncertainty age model (Myr)	Global uncertainty (Myr)	Duration (Myr)
LO <i>L. bolli</i>	Base NC5C	14.9		126.63	0.13	0.23	1.42
LO <i>M. spinulentus</i>		20.3		125.61	0.08	0.21	
LO <i>C. oblongata</i>	Base NC5D	41.4		125.21	0.12	0.22	0.66
FO <i>F. oblongus</i>	Base NC5E	57.9		124.55	0.11	0.22	2.15
FO <i>L. sp. cf. L. magnus</i>		72.1	11.7	123.57	0.11	0.22	
FO <i>M. stellatus</i>			32.7	122.64	0.10	0.21	
FO <i>H. irregularis</i> E	Base NC6A		41.4	122.40	0.05	0.20	N.A.
FO <i>H. irregularis</i>			46.1	122.16	0.14	0.24	

**Table 3.** Ages and durations of calcareous nannofossil events and subzones

Episode	Level at Arroyo Gilico (m)	Level at Barranco Cavila (m)	Numerical age (Ma)	Uncertainty age model (Myr)	Global uncertainty (Myr)	Duration (Myr)
Faraoni Level base	13.6		126.70	0.12	0.22	0.10
Faraoni Level top	15.5		126.60	0.13	0.23	
Mid-Barremian Event base	54.0		124.68	0.10	0.21	0.46
Mid-Barremian Event top	63.0		124.22	0.15	0.24	
Taxy Event base		44.2	122.25	0.11	0.22	0.87
Base of Latest Barremian $\delta^{13}\text{C}$ excursion		50.6	121.93	0.11	0.22	
Taxy Event top		62.2	121.38	0.12	0.22	

**Table 4.** Ages and durations of the Episodes of Environmental Change of the Late Hauterivian–Barremian